



Politecnico di Torino

Department of Environmental, Land and Infrastructure Engineering

Master of Science in Petroleum and Mining Engineering

Numerical modelling of Balçova-Narlıdere geothermal field, Izmir, Turkey

Candidate: Nijat Ismayilov (272612)

Supervisors:

Prof. Glenda TADDIA

Prof. Alper BABA (Izmir Institution of Technology)

Co-supervisors:

Dr. Martina GİZZİ

Dr. Taygun UZELLİ (Izmir Institute of Technology)

Academic Year 2021/2022

Thesis submitted in compliance with the requirements for the Master of Science degree in
Petroleum and Mining Engineering

ABSTRACT

Since Turkey is located on an active tectonic belt due to its geological and geographical location, it is in a rich position among the countries of the world in terms of geothermal energy. The Balçova-Narlıdere Geothermal Field (BNGF) is located on the southern edge of Izmir Bay of the Aegean coast and is 11km far from southwest of Izmir city. This geothermal play represents the first field in Turkey used for the application of direct heating. Beginning in 1960, studies about hydrogeology, hydrochemistry, reservoir performance, temperature analysis and use of geothermal water are still going on in the Balçova-Narlıdere Geothermal field. Currently, there are 26 wells drilled by Izmir Geothermal Energy Company in the field. Among 26 wells, 11 are deep production wells, 5 wells are shallow production wells, 4 wells are re-injection wells, 4 wells are gradient wells for research goals and the rest 2 wells are not feasible to utilize. There was a renewal of six wells from 2013 to 2015. Besides these 26 wells, there are additional 11 wells drilled which belong to Izmir Governorship Investment Monitoring and Coordination Department. Shallow wells correspond to depths up to 200m, while deep wells range from 410m to 1100m depth. The energy obtained from Balçova-Narlıdere Geothermal field has been supplied to approximately 38500 residences, beginning from 1996.

A numerical simulation of the Balçova-Narlıdere Geothermal field has been implemented to predict the future reservoir performance regarding temperature and pressure states. Model construction, natural state modelling using EOS1 in BNGF and history match of injection and production data are stages of simulation conducted prior to future reservoir performance forecasting. The performance prediction has been carried out according to three production/injection scenarios.

In the Scenario-I, the production and injection flow rates have been kept the same for next 20 years beginning from 2008. In Scenario-II, the simulation has been carried out for 15 years' period. Initially, the production and injection rates remain the same for the first three years, after which they have been increased by 10% and 17%, respectively, every three years. Scenario-III includes a new BT-1 well drilled at depth of 765m to operate as an injection well from the start of the simulation. Here, about 60 percent of injected water through well BD-8 has been transferred to newly operating well BT-1. Scenario-III has the same production scenario as Scenario-II.

From the results of all three scenarios, it can be deduced that there is no important change in bottomhole pressure in deep wells. However, in Scenario-II and III shallow wells B-5 and B-10 represented pressure drop. By comparing the first two scenarios, Scenario-I is more feasible as in the Scenario-II temperature of deep wells in the field was reduced more than in Scenario-I. Having

said that, in Scenario I, the temperature in the eastern side deep wells reduced significantly while in the western side deep wells decreased less, in comparison with deep wells in Scenario-III.

Keywords: Balçova-Narlıdere Geothermal Field, Numerical simulation, Natural State Modelling, Hydrogeology, Hydrochemistry.

ACKNOWLEDGEMENTS

I am thankful to Prof. Alper BABA from Izmir Institute of Technology (Iztech) for supervising me under this project and helping me in data supply that made this project possible. I would like to acknowledge and express my heartfelt gratitude to Prof. Glenda TADDIA for allowing me to participate in the outgoing mobility program, which turned out to be an unforgettable and one-of-a-kind event in my life.

I would also like to give special thanks to Dr. Martina GIZZI and Dr. Taygun UZELLI from Izmir Institute of Technology for their guidance and support which progressed me through all the steps of writing this project.

Moreover, especially, I wish to acknowledge the outstanding help of Izmir Geothermal Energy Company Inc. in providing necessary data regarding field experience. In addition, my thanks to Iztech Life Center for supplying me with the accommodation throughout the research period.

I am also grateful so much to professors of Department of Environment, Land and Infrastructure for teaching, providing priceless education during the journey I experienced in Polytechnic University of Turin.

Ultimately, I need to express my sincere gratitude to my beloved family for their love, care, motivation and support in any condition in my life.

TABLE OF CONTENTS

ABSTRACT.....	2
ACKNOWLEDGEMENTS	4
LIST OF TABLES	7
LIST OF FIGURES	8
LIST OF SYMBOLS	9
CHAPTER 1: INTRODUCTION.....	10
1.1 The objective and scope of research.....	10
1.2 Geothermal energy and its use.....	10
1.3 Geothermal potential in Turkey	10
CHAPTER 2: LITERATURE REVIEW.....	13
2.1 Geolocation of BNGF.....	13
2.2 Tectonic and geological framework of BNGF	14
2.2.1 Regional Geology	14
2.2.2 Stratigraphic units of BNGF	16
2.2.2.1 Bornova Complex	18
2.2.2.2 Alluvium	19
2.2.3 Tectonics and structural geology of BNGF.....	21
2.2.3.1 Izmir Fault.....	23
2.3 Conceptual model	25
2.4 Well properties in BNGF.....	27
2.5 Hydrogeochemistry of geothermal fluid in BNGF	32
2.5.1 Physical properties of geothermal water.....	32
2.5.2 Chemical properties of geothermal water.....	34
CHAPTER 3: PROBLEM STATEMENT	39
CHAPTER 4: METHODOLOGY.....	40
4.1 TOUGH2 software	40
4.2 Modules of Equation of State.....	41
4.2.1 EOS 1.....	41
4.2.2 EOS 2.....	41
4.2.3 EOS 3.....	41

4.2.4 EOS 4.....	41
4.2.5 EOS 5.....	42
4.3 Petrasim	42
4.4 Model construction	42
4.5 Natural state modelling	43
4.6 History matching.....	44
4.7 Forecasting	44
CHAPTER 5: RESULTS AND DISCUSSION	47
5.1 Model construction	47
5.2 Natural state modelling	48
5.3 History matching.....	54
5.4 Production and reinjection data history	57
5.5 Forecasting	58
CHAPTER 6: CONCLUSION.....	63
REFERENCES.....	65

LIST OF TABLES

- Table 1. Wells and their characteristics in BNGF.
- Table 2. Lithological intervals crossed by geothermal wells.
- Table 3. Major anion-cation measurements at the sampling points determined in the Balçova geothermal area.
- Table 4. Material properties within the model.
- Table 5. Cumulative amount of water produced and reinjected in BNGF in years between 2014-2021.

LIST OF FIGURES

- Figure 1. Geothermal resource areas and temperature distribution in Turkey.
- Figure 2. The location of Balçova-Narlıdere geothermal field according to Google Earth map.
- Figure 3. Regional map displaying the major neotectonic structure of Turkey.
- Figure 4. Location of the study area on the regional geological map.
- Figure 5. Generalized lithostratigraphic column section of the study area and its surroundings.
- Figure 6. Field images of Bornova Complex.
- Figure 7. Panoramic terrain photograph showing young depositional areas in the south of Izmir Bay.
- Figure 8. Colluvial deposits made of coarse clastic sediments with no internal organization and poor textural characteristics.
- Figure 9. Field photograph of the convergent section of coarse clastic alluvial fan deposits.
- Figure 10. Substantial elements controlling Balçova-Narlıdere geothermal system.
- Figure 11. Active fault map showing the relationship between the Izmir Fault and the Study Area.
- Figure 12. 3D image of conceptual model of BNGF created by means of Leapfrog software.
- Figure 13. Fault segments demonstration of BNGF.
- Figure 14. The pathways (thin red lines) through which geothermal water reaches the surface.
- Figure 15. Depths of geothermal wells in BNGF.
- Figure 16. Temperature distribution in BNGF.
- Figure 17. Electric Conductivity (EI) values derived from analysis of geothermal fluid sampled from production and re-injection wells in 2020, 2021, 2022.
- Figure 18. pH values derived from analysis of geothermal fluid sampled from production and re-injection wells in 2020, 2021, 2022.
- Figure 19. Cl⁻ values of production wells and re-injection wells in the Balçova-Narlıdere geothermal field.
- Figure 20. Production/injection well scheme for Scenario-I.
- Figure 21. Production/injection well scheme for Scenario-II.
- Figure 23. Production/injection well scheme for Scenario-III.
- Figure 24. 2D grid model results displaying rock, fault and air distribution at various cross section.
- Figure 25. Distribution of modelled and measured temperature values with depth for shallow and deep wells.
- Figure 26. Comparison between modelled and measured temperature values at natural state.
- Figure 27. Temperature distribution at natural state in BNGF at various cross sections.
- Figure 28. The Distribution of modelled and measured temperature values for shallow and deep wells for 13 years period.
- Figure 29. Comparison between modelled and measured temperature values during production-injection period.
- Figure 30. Bottomhole temperature results derived from simulation run for all three scenarios.
- Figure 31. Bottomhole pressure results derived from simulation run for all three scenarios.

LIST OF SYMBOLS

BNGF	Balçova-Narlıdere Geothermal Field
°C	Degrees of Celsius
WAEP	Western Anatolian Extensional Province
IBTZ	Izmir Balıkesir Transfer Zone
IF	Izmir Fault
FS	Fault segments
EC	Electrical conductivity
EOS	Equation of State
P	Pressure
T	Temperature
S_g	Gas phase saturation
P_g	Gas phase pressure
P_{CO2}	Carbon dioxide partial pressure
AG-I	Agamemnon-I Fault
AG-II	Agamemnon-II Fault
AG-III	Agamemnon-III Fault

CHAPTER 1: INTRODUCTION

1.1 The objective and scope of research

This research is purposed to implement the numerical modelling of Balçova-Narlıdere geothermal field and make future predictions based on this model in order to estimate the geothermal reservoir performance for the next several years. Moreover, a conceptual model, geothermal water analysis, hydrogeochemical and hydrogeological investigations of the field have been considered as other primary objectives of the study.

1.2 Geothermal energy and its use

Geothermal Source represents the places, where depending on the geological structure, with the effect of the Earth's crust heat, the temperature is constantly above the regional atmospheric annual average temperature, which may contain more dissolved substances and gases than the surrounding waters, naturally emitted or extracted water, steam and gases, and they are sent underground through human arrangements. These sources can be referred as the places where water, steam and gases are obtained by heating with the heat of the crust or hot dry rocks. The energy obtained from such sources is called "geothermal energy".

Today, most of the energy produced in the world is derived from fossil fuels such as oil, natural gas, coal and nuclear energy. Furthermore, there are sustainable and eco-friendly resources, i.e., sunlight, wood, wind, geothermal and hydroelectric. (Kömürçü & Akpinar, 2009)

Utilization of clean and renewable energy resources like geothermal energy has been increasing worldwide considering deleterious effects on the environment because of combustion of fossil fuels. Geothermal energy being safe and clean and having a low environmental impact is one of the best renewable energy sources for power generation, cooling and heating. (Kömürçü & Akpinar, 2009)

1.3 Geothermal potential in Turkey

Since Turkey is located on an active tectonic belt due to its geological and geographical location, it is in a rich position among the countries of the world in terms of geothermal. There are many geothermal resources at different temperatures in the form of around 1000 natural outflows spread all over Turkey. The geothermal potential of Turkey is quite high, where 78% of the potential areas are in Western Anatolia, 9% in Central Anatolia, 7% in the Marmara Region, 5% in Eastern Anatolia and 1% in other regions. According to (*MTA Genel Müdürlüğü*, 2022), about 90% of geothermal resources in Turkey are low and medium temperature and suitable for direct applications (heating, thermal tourism, various industrial applications, etc.), while 10% are suitable for indirect applications (electric power generation).

Geothermal resources have widespread use. Today, geothermal energy obtained in Turkey is utilized in several fields such as electricity production, heating (greenhouse and housing), thermal and health tourism, industrial mineral extraction, fishing, drying etc. The first electricity generation in Geothermal Energy applications was initiated in 1975 with the Kızıldere Power Plant, which was established by the General Directorate of MTA and has a power of 0.5 Mwe. (*MTA Genel Müdürlüğü*, 2022)

According to the data to the end of 2018 derived from General Directorate of MTA, the installed power of geothermal energy in the world is at the level of 14.9 Gwe. USA, Philippines Indonesia, Turkey and New Zealand are top five countries in electricity generation from the geothermal energy source. Non-electrical consumption has exceeded 70Gwt and the countries in the direct use applications in the world are the USA, China, Sweden, Belarus and Norway. (*MTA Genel Müdürlüğü*, 2022)

The exploration and discovery of geothermal resources were initiated by the General Directorate of MTA in 1962, and high-temperature geothermal resources reaching temperatures up to 287.5°C were identified. The geothermal energy exploration activities, which had stopped due to the policies implemented from the 1990s until 2004, were accelerated and the amount of budget dedicated for exploration of geothermal energy sources were increased by ten times. Since 2005, with the support of our Ministry, due to the development of existing resources and the search for new resource areas, the usable heat capacity, which was 3100 MWt as of the end of 2004, increased to 5000 MWt as of the end of December 2018. (*MTA Genel Müdürlüğü*, 2022)

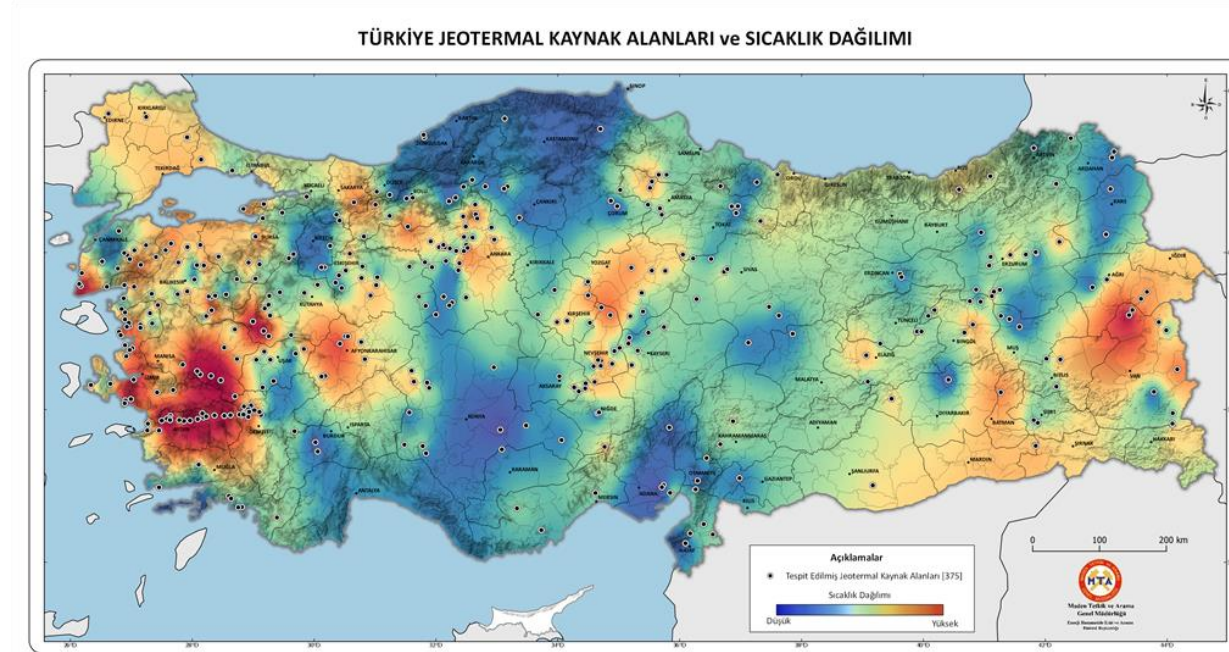


Figure 1. Geothermal resource areas and temperature distribution in Turkey (*MTA Genel Müdürlüğü*, 2022).

CHAPTER 2: LITERATURE REVIEW

2.1 Geolocation of BNGF

The Balçova-Narlıdere geothermal field is on the southern edge of Izmir Bay of the Aegean coast and is 11km far from the southwest of Izmir city. The Mediterranean climate is a beneficial aspect for Balçova field in terms of warm, rainy winters and hot, dry summers. The district, which hosts both local and foreign tourism activities, has a predominantly Mediterranean climate, which influences different plant communities. Balçova's natural beauty is mostly based on a 500 m elevation area and the coastline's gentle sloping towards the shore. Additionally, Agamemnon Thermal Springs draw a sizable number of visitors from abroad to the region.

İlica Stream is located in the Balçova-Narlıdere geothermal field. İlica Creek has a continuous flow. The flow rate is high, especially in rainy periods. In dry periods, the flow rate is very low. İlica Stream can be affected by all kinds of pollution. Except for the İlica creek, other surface water structures are generally seasonal.

The Balçova geothermal field has been the subject of hydrogeological, geological, and geothermal studies since 1960. These investigations encouraged both the public and private sectors to drill producing and research wells in the region. There are mainly two reservoirs existing in the field. One of them is a shallow reservoir where wells are drilled at a depth lower than 200 meters and the other one is a deep reservoir where wells' depth range is between 410 and 1100m. The temperature in the reservoir ranges from 60°C to 140°C.



Figure 2. The location of Balçova-Narlıdere geothermal field according to Google Earth map (Baba et al., 2022).

2.2 Tectonic and geological framework of BNGF

This section provides information on the geology of Balçova-Narlıdere geothermal field. Then, the stratigraphic and structural features of the study area are examined in detail.

2.2.1 Regional Geology

The area of research is in the Western Anatolian Extensional Province (WAEP). Here, Eocene sedimentary rocks, Paleozoic-Mesozoic rocks (Cyclades and the Menderes Massif, rocks of the 'İzmir-Ankara Zone), Plio-Quaternary units and Neogene volcanic sedimentary rocks are found. The province is described by east-to-west (E-W) trending graben structures which are derived from the northeast-to-southwest (NE-SW) trending Izmir Balikesir Transfer Zone (IBTZ) (Figure 3). (Gessner et al., 2013) (Baba et al., 2022) According to studies carried out recently, African Plate underlying the western Anatolian crust is being rifted causing the IBTZ in the Western Anatolian crust to develop along the surface. Hence, surface fracturing led to the development of a brittle shear zone between Izmir (Gümüldür) and Balikesir (Bigadiç), dominated by E-W trending normal faults and NE-SW and NW-SE trending strike-slip faults. The IBTZ represents a brittle shear zone of 150 km length dominated by Late Cretaceous. (Baba et al., 2022) (Sözbilir et al., 2011)

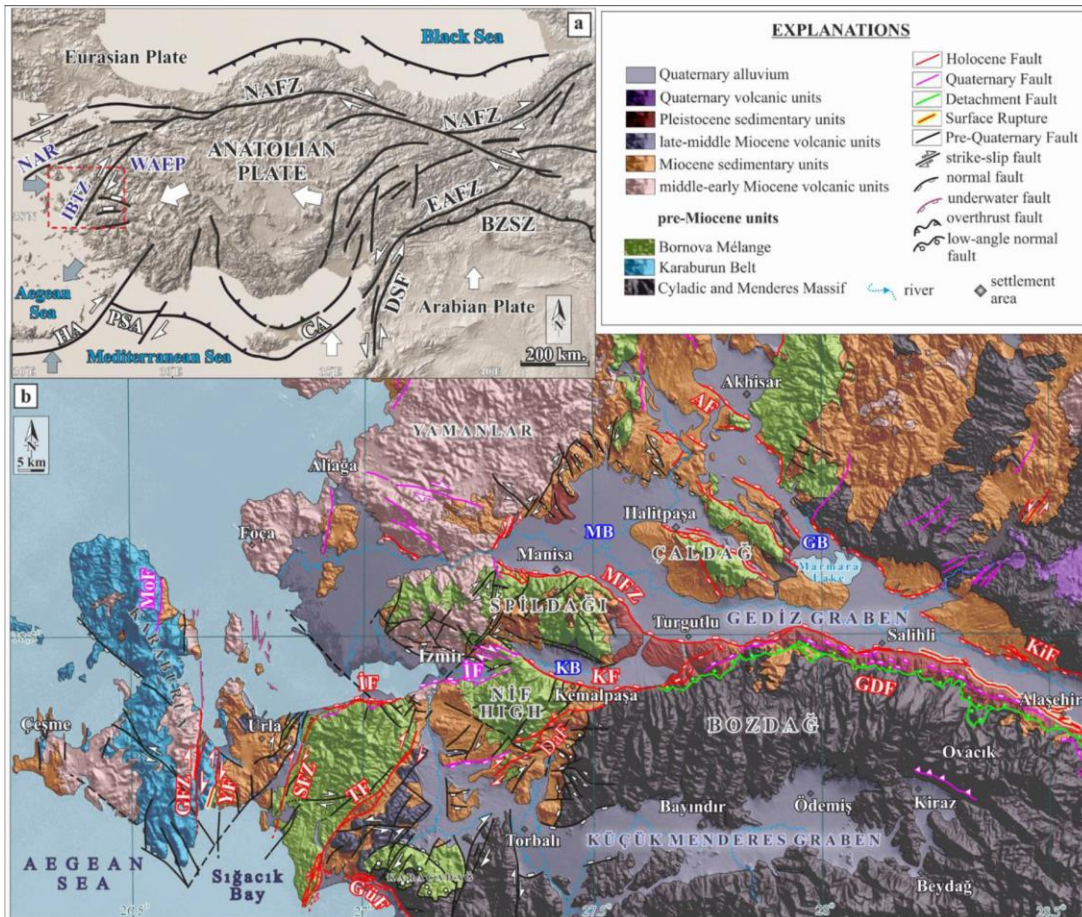


Figure 3. Regional map displaying the major neotectonic structure of Turkey (Tepe et al., 2021).

The Kocaçay Basin, which stretches between Kemalpasa and Torbali, forms the zone's eastern border, while the Karaburun Zone forms its western margin. The primary structural components on the zone's western border are the boundary faults of the Urla Basin, which is situated between the Karaburun Zone and Seferihisar Horst. Volcanic and lacustrine basins that formed at Cumaovasi, Yamanlar, Yunt Mountain provide evidence of the region's activity during the Miocene. (Baba et al., 2022) The IBTZ developed like an accommodation zone between the inner bay of Izmir and Kemalpasa basin. The section of the IBTZ that is located south of Gümüldür extends along Kusadas Bay under the Aegean Sea. Numerous active faults within the area can be seen by the earthquakes that have occurred along the zone during the previous 100 years. The inner bay of Izmir and Seferihisar Horst, where the BNGF is situated, are structurally separated by one of these faults, the Izmir Fault.

Located on the rising block of the Izmir Fault, the Seferihisar Horst is made up of the Late Cretaceous-Paleocene aged Bornova Complex, which is limited by faults on three sides. Bornova Complex, which is composed of a matrix consisting of sandstone-mudstone alternation and

limestone blocks in sizes that can be mapped in this matrix, is cut by the Oligocene aged Granodiorite unit (Figure 4).

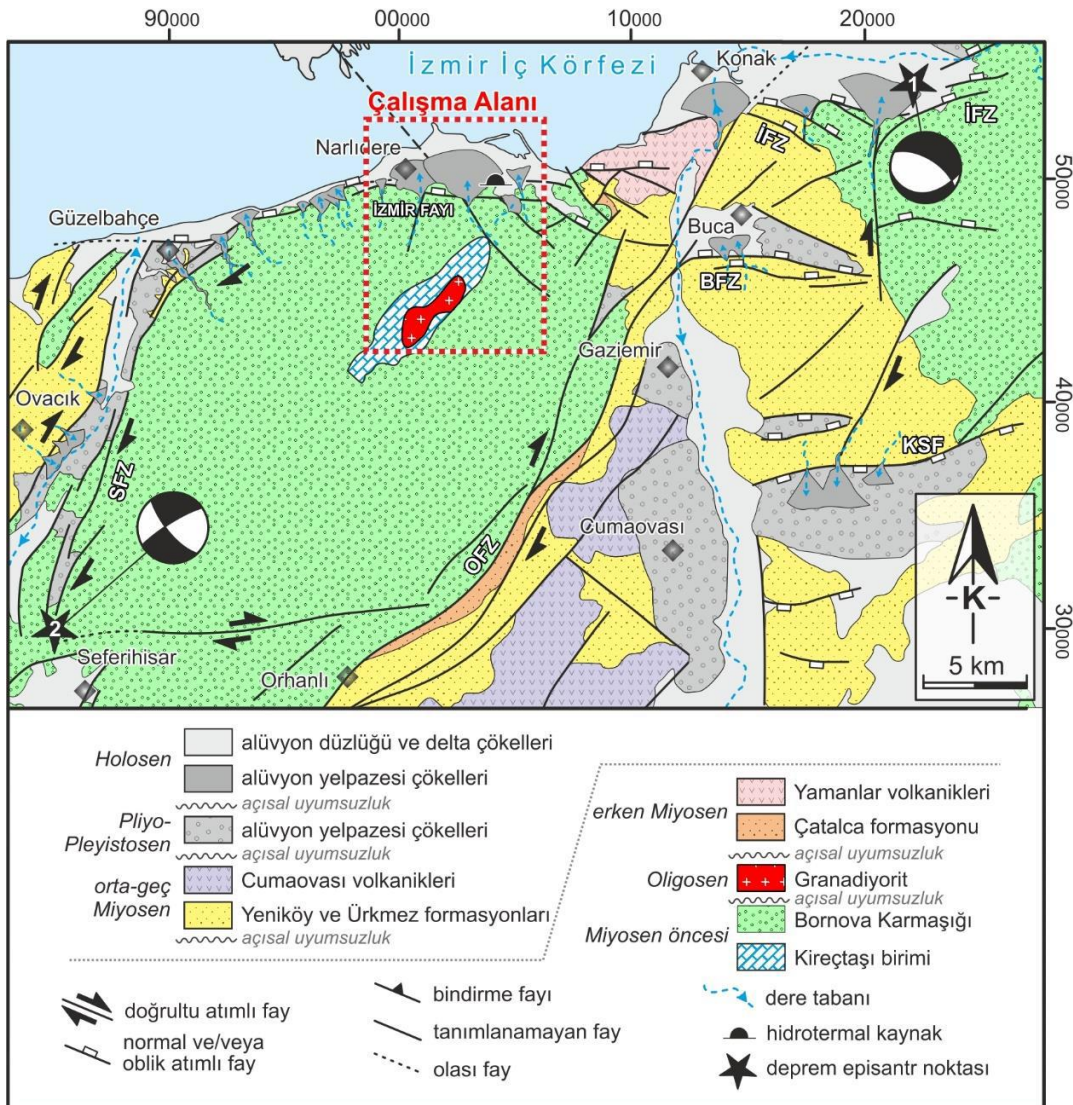
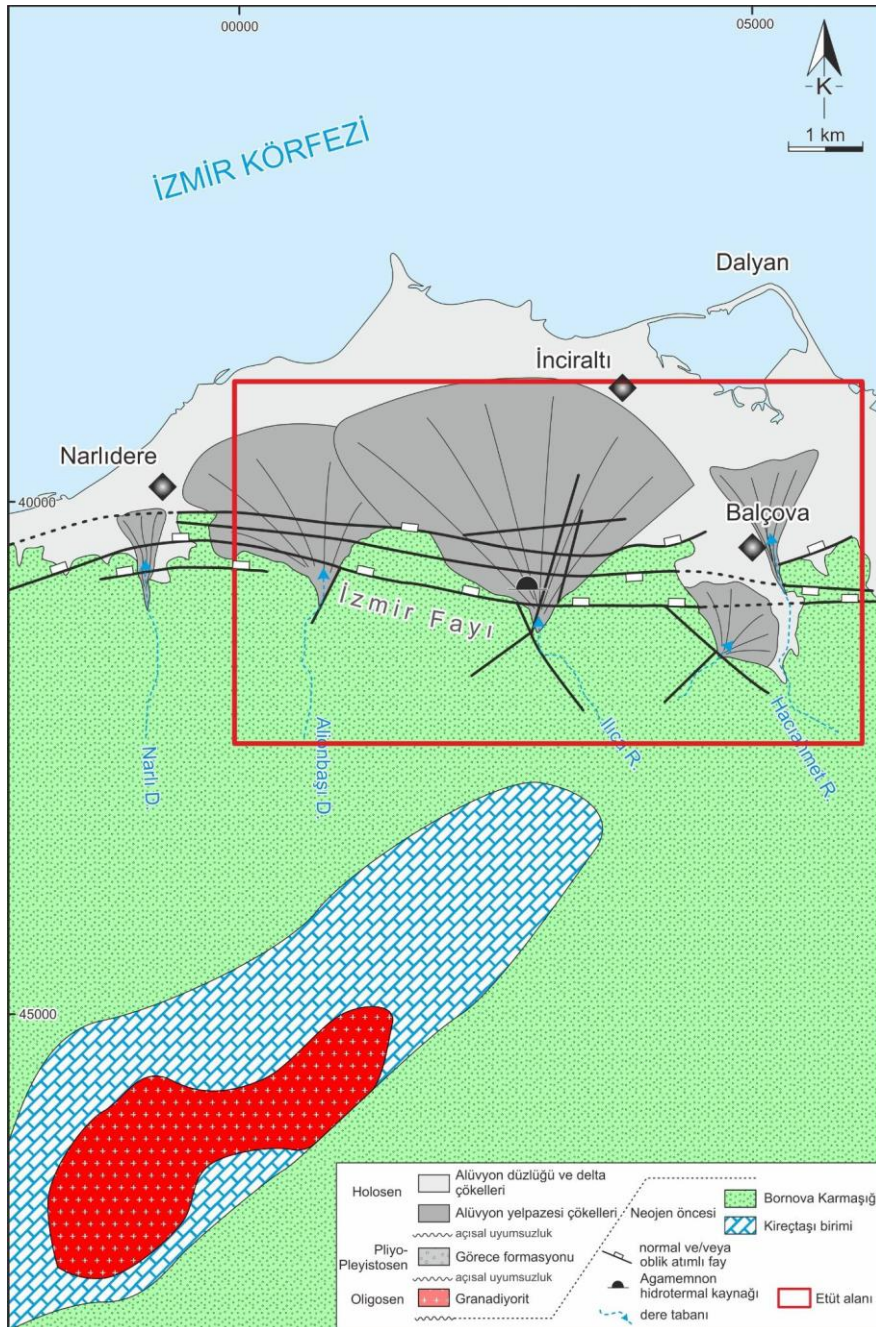


Figure 4. Location of the study area on the regional geological map (Uzel et al., 2012)

2.2.2 Stratigraphic units of BNGF

The study area is located at the midpoint of the Narlidere and Balçova district settlements on the southern edge of the Izmir Inner Bay, which has an approximate E-W trend, limited by the Gediz Delta and Yamanlar Elevation from the north and the Seferihisar Elevations from the south. Within the boundaries of the study area, there are two rock units separated from each other by a main unconformity. Considering their geological ages and stratigraphic positions, these are Late Cretaceous-Paleocene aged Bornova Complex and Quaternary-Holocene Alluvial deposits from bottom to top, respectively (Figure 5). It is cut by the Oligocene granodiorite south of the Bornova Complex area. The Bornova Complex is cut by the Oligocene granodiorite in the south of the area.



Yaş	Birim	Kalınlık (m)	Litoloji	Açıklama
Geç Kretase-Paleosen	Alüvyal Çökeller	~15		Alüyon düzluğu-delta çökelleri: kil ve silt ara maddeli pekleşmemiş kum Akarsu kanal çökelleri: kötü boyanmış, yer yer çapraz katmanlı, pekleşmemiş çakıl ve kum Alüyon yelpazesi çökelleri: kötü boyanmış, ara madde destekli çakıl ve kum açışal uyumsuzluk kumtaşı-çamurtaşı ardalanması kireçtaşları bloğu mikritik kireçtaşları merceği çakıltaşları merceği spilitik volkanit
	Bornova Karmaşığı	?		Oligosen granodioriti

Figure 5. Generalized lithostratigraphic column section of the study area and its surroundings
(Hasan SÖZBİLİR & Prof. Dr. BABA, 2016).

2.2.2.1 Bornova Complex

According to (Burhan Erdogan, 1990), the Bornova Complex is made up of recrystallized limestone, serpentinite, chert and mafic volcanites of different sizes within a matrix of sandstone, mudstone, and mudshale alternations and lenticular micritic limestones. In the study area, the units forming the matrix of the Bornova Complex are dominantly observed. The units constituting the matrix of the Bornova complex can be classified as sandstone, mudstone and mud shale lithologies according to their dominance ratios. Scattered and small amounts of recrystallized limestone and sandstone blocks in mesoscopic scale are also observed in this matrix. The sandstones are grayish yellow – brownish burgundy, thin and medium bedded and have medium high strength (Figure 6). Mudstones, on the other hand, are generally observed in thin bedding and have low medium strength. Greenish gray, grayish brown mud-shales are of low strength.



Figure 6. Field images of Bornova Complex

The matrix made of fine clastic sedimentary rocks, reflecting the characteristics of the flysch facies laterally and vertically, contains extremely dense deformation structures due to tectonism. For this reason, the primary layer structures of the unit, which presents variability in terms of lithology and strength at very short distances, are observed to be distorted. Though the bedding of the units that make up the matrix is not consistently observed in a regular pattern, it has been noted that around the southernmost border of the research region, these fine-clastic sedimentary units often strike in a north-south direction and dip in a north-south direction varying by 35° to 80° .

Within the boundaries of the research area, the lower contact of the Bornova Complex cannot be seen. On a regional level, it is known that the Menderes Massif's metamorphic rocks and the Complex's lower contact are in tectonic contact (Başarır & Konuk, 1981), (Burhan Erdogan, 1990), (Sözbilir et al., 2011). Quaternary-Holocene-aged sediments in the study area unconformably cover the unit's upper stratigraphic contact (Figure 6). Generally, in the literature the Bornova Complex's age is indicated as the Upper Cretaceous to Paleocene, particularly with the help of plaque-tonic foraminifera found in its matrix (Burhan Erdogan, 1990) (Sari, 2013).

2.2.2.2 Alluvium

Less compacted sedimentary rocks and/or clastic deposits that are still undergoing sedimentation make up the Quaternary-Holocene aged units outcropping in the research area. The sediments assigned to this title were divided into three major sediment packs based on their distribution zones, morphologies, observational limits, and the features of the current environment they reflect. These sediment groups are Alluvial plain deposits, Colluvial deposits and Alluvial fan deposits. Although there are few outcrops in the field where these stratigraphic relationships can be seen, the borders of these strata, which make up the major rock unit of the research area, can be determined by taking into account morphological features and contemporary environmental areas (Figure 7). (Baba et al., 2022)



Figure 7. Panoramic terrain photograph showing young depositional areas in the south of Izmir Bay.

The data derived from well logging in the study area demonstrate that these units' thickness is more than 15 meters in certain places and they unconformably overlie the fine clastic sediments of Bornova Complex near the southern boundary of the study region. These sediments consist of blocky and inter-clay grains, poorly sorted - very poorly, unconsolidated and/or under-consolidated, coarse clastic, poorly textural clastic sediments with generally single type of grain components (Figure 8). (Baba et al., 2022)



Figure 8. Colluvial deposits made of coarse clastic sediments with no internal organization and poor textural characteristics

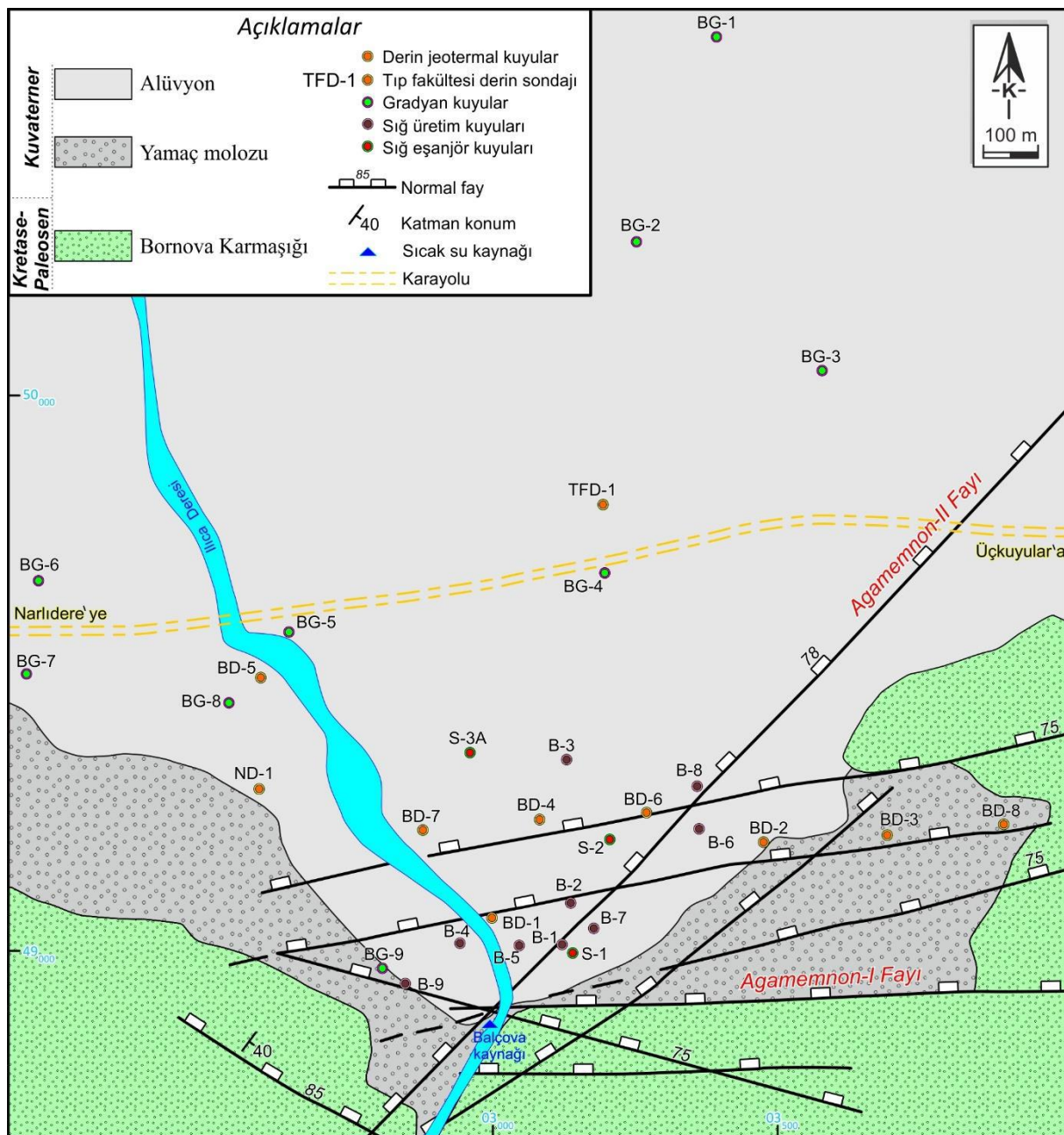
On the other hand, alluvial fan deposits are made up of clastic sediments that are dark light brown, reddish orange, and have grain sizes that range from block to sand. These deposits are generally composed of coarse conglomerate, pebbly sandstone and coarse sandstone with intermediate and partly grain supported, poorly weathered, poorly medium rounded blocks. Blocks and pebbles are predominantly composed of sandstone, limestone and quartzite components. Sedimentary structures observed in the coarse-mid-clastic organized parts of these deposits indicate that the dominant flow direction is NNE (Figure 9).



Figure 9. Field photograph of the convergent section of coarse clastic alluvial fan deposits (red dashed lines show the estimated transitional boundaries of the current depositional areas, red arrow indicates the direction of the stream, the average height of the people in the photographs is 160-170 cm).

2.2.3 Tectonics and structural geology of BNGF

The major structural elements in the İzmir-Balçova-Narlıdere geothermal area are the geothermal system controlling faults and folds. İzmir Fault (IF) is the main fault in the region bordering İzmir Bay from the south. According to old studies, Agamemnon-I fault is known as one of the branches of the İzmir Fault. There are NE-SW and NW-SE trending faults that are cut by İzmir Fault (Figure 10). Here, the NE-SW trending fault is also known as Agamemnon-II fault which crosses İlica Greek.



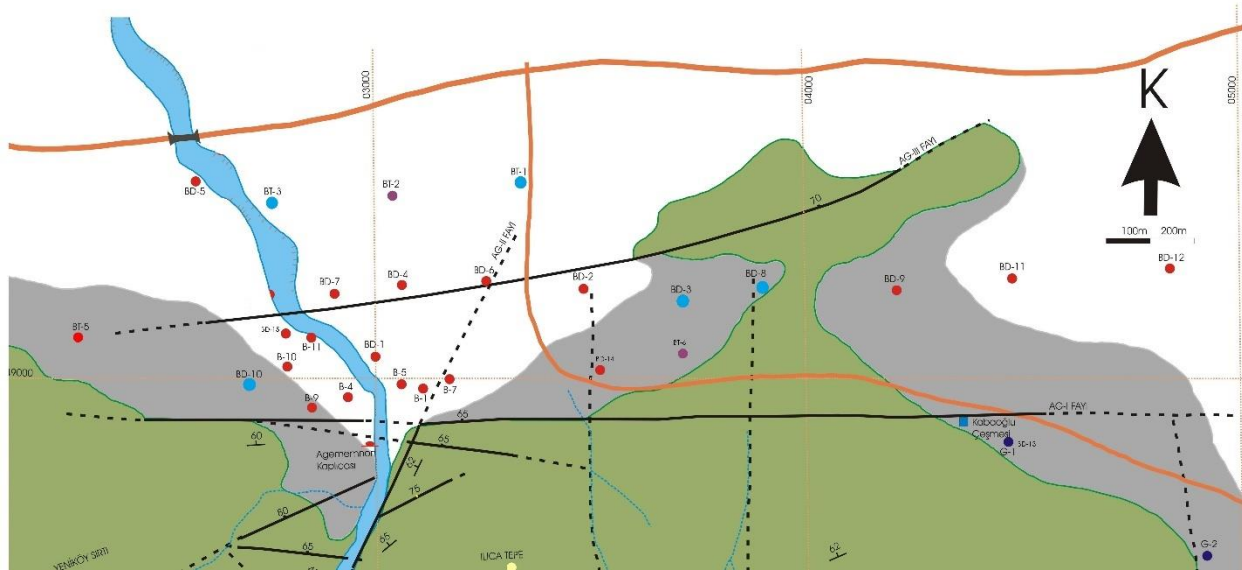


Figure 10. Substantial elements controlling Balçova-Narlıdere geothermal system (Hasan SÖZBİLİR & Prof. Dr. BABA, 2016)

2.2.3.1 Izmir Fault

Izmir Fault with the length of 40km (35km onshore and 5 km offshore) forms the structural boundary between Izmir Bay and Seferihisar Ascension (Uzel et al., 2012). Izmir Fault (IF) starts in the east from Pınarbaşı and extends westward to Üçkuyular. There are fault segments of the Izmir Fault extending E-W which continue towards Balçova and Narlıdere and reach Güzelbahçe via low-wavelength curved extension (Sözbilir et al., 2008).

In the rising block of the fault, the Upper Cretaceous–Paleocene Bornova Complex, Miocene aged volcano sedimentary units are defined and in the falling north block, Quaternary-Holocene aged alluvial, sediments in which fluvial and marine inputs are found out and sandstone-shale belonging to Bornova Complex outcrops are observed. The exposure of Bornova Complex in the ceiling block of the fault is based upon the antithetic and synthetic segments of Izmir Fault's ceiling block. In the section of Izmir Fault between Balçova and Güzelbahçe, alluvial fans with their axis extending in approximately NE direction have developed, and these fans show a transition to fan delta-coastal deposits towards Izmir Bay (Sözbilir et al., 2008) .

Among the NE-SW and NW-SE trending faults, NE strikes are dextral strike-slip faults with high dips and low rake angles, while NW-trending lines are left lateral strike-slip faults with rake angles of 20-30°. Geomorphological indices such as fore-mountains lineaments, alluvial fans, under-iron structures and drainage networks that are observed along the Izmir Fault in Balçova and its western part indicate that the Izmir Fault was active in the Holocene as a normal fault(Sözbilir et al., 2008).

According to (Emre et al., 2005), the western part of Izmir Fault is divided into two geometric segments named Balçova and Narlıdere, taking into consideration the change in direction and the jump geometry between the subsections of the fault. In agreement with researchers, the Balçova segment strikes N82°E and is 15 km long. The Balçova segment is the best geologically and geomorphologically observable part of the Izmir Fault. At the western end of fault, it bifurcates into two directions. The southern branch terminates in the direction of the NE-SW trending and right-lateral strike-slip Seferihisar Fault. The northern branch heading towards NW is probably connected with the fault zone in the NNW-SSE direction located in the east of Çiçekadaları and Uzunada at the base of Izmir Bay. Studies carried out in the west of Izmir Bay indicate that there is NNW-SSE trending tectonic depression in the east of Uzunada and the faults controlling this depression cut the Quaternary sediments.

There are Miocene aged volcanic and sedimentary rocks existing in the southern block of the fault between Balçova and Buca. The Pliocene erosional plains developed on these rock assemblages in the Buca region were cut by the Izmir Fault and suspended in the southern block of the fault. Moreover, the basement rocks are forming Nif Mountaing rise in the southern block of the Pınarbaşı region. Multi-period valley scrapings or splits are evident in the riverbeds that are located on the uplifts in the southern block of the fault and flowing to the north. This morphotectonic structure observed along the fault indicates a general regional tectonic uplift in the southern block of the Izmir Fault, which developed after the Pliocene(Emre et al., 2005).

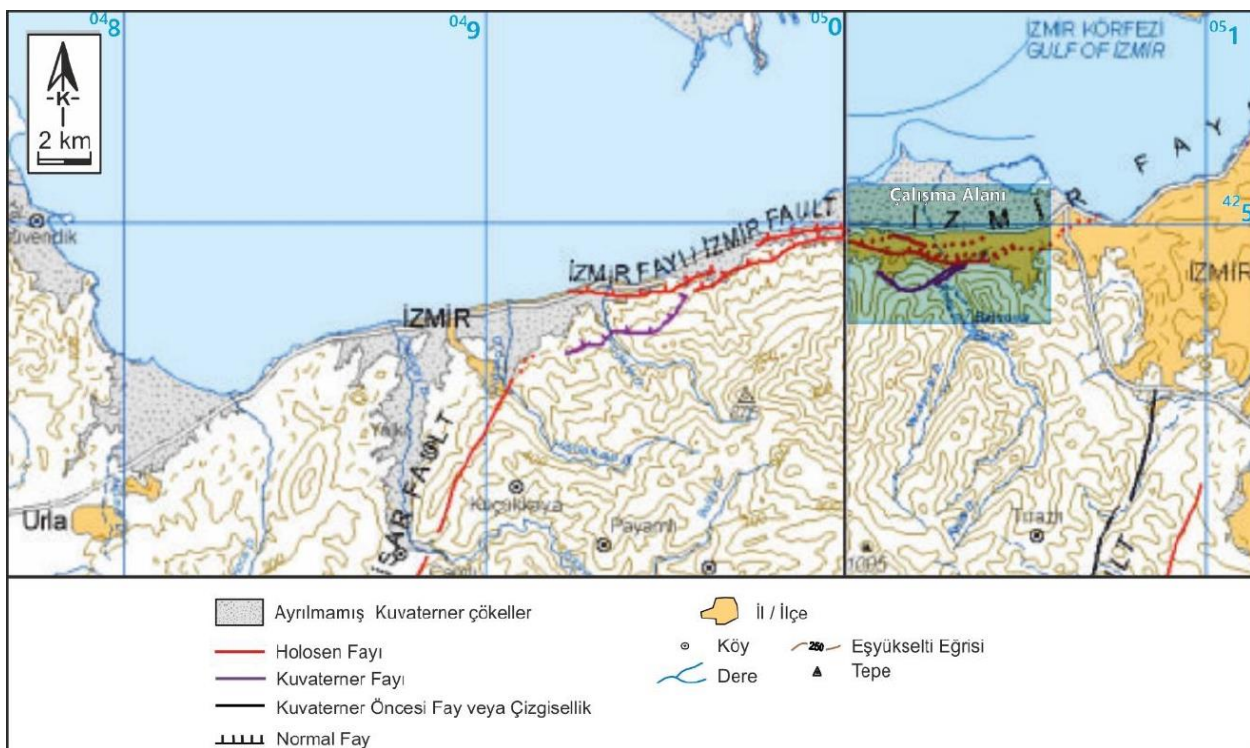


Figure 11. Active fault map showing the relationship between the Izmir Fault and the Study Area
(Hasan SÖZBİLİR & Prof. Dr. BABA, 2016)

2.3 Conceptual model

The conceptual model has been developed for Balçova-Narlıdere geothermal system, where tectonics and lithological structure, temperature distribution, geothermal water pathways and well location indication are represented in the 3D model form to visualize the geothermal system in the best way. The model also helps to develop numerical modelling studies in the next steps. In the (Figure 12), the lithological and structural features along with 19 wells are displayed within conceptual model of BNGF system. The conceptual model was conducted using Leapfrog Sequent Software.

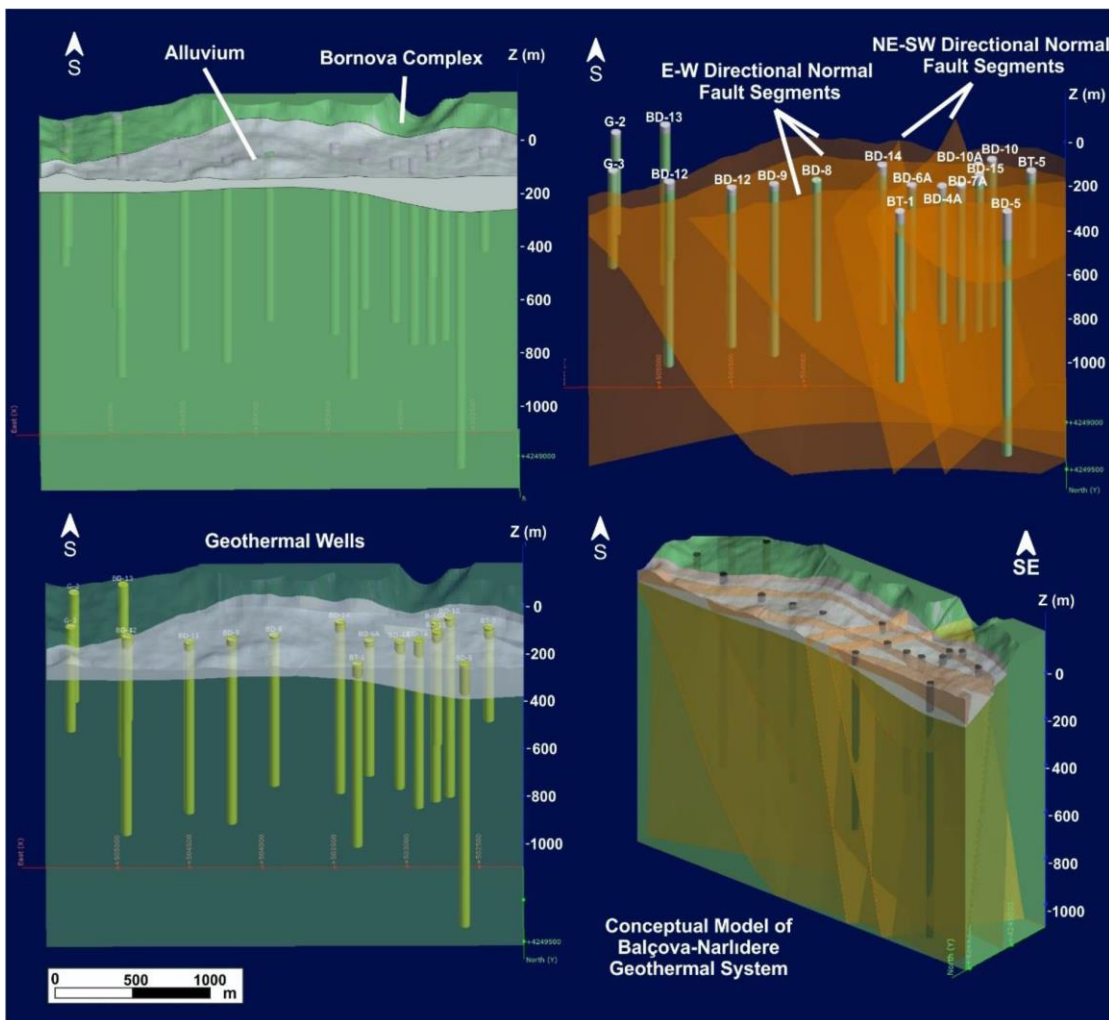


Figure 12. 3D image of conceptual model of BNGF created by means of Leapfrog software (Baba et al., 2022)

Mainly, the BNGF is situated on the active IF and its segments. Izmir Fault comprises four normal major segments trending in EW direction and two normal segments trending in NE-SW direction (Figure 13). It can be seen from the model the E-W fault segments are FS-1, FS-2, FS-3, FS-4, while NE-SW segments are FS-5 and FS-6. Moreover, fracture-crack systems that have evolved inside the basement units and comparatively smaller fault segments in the E-W and N-S directions are two additional significant structural features in the area. Overall, these faults segments constitute a geothermal play and can be considered as significant structural controls of the field. Almost all the deep wells intersect Izmir Fault with these fault segments which are connected to joints and fracture zone of about 2km length. These faults segments divided the field into footwall block where Bornova Complex units mainly exist and hanging wall block consisting of fluvial, Quaternary-Holocene, marine, alluvial units. From (Sözbilir et al., 2008), it has been seen in footwall block that left-lateral and right-lateral strike slip faults correspond to NW and NE trending faults, respectively. The rake of angle of these faults are nearly in the range of 20-30°. According to the analysis made on the study area about Izmir fault, the range of strike of the fault varies from N60°W to N85°E. Moreover, field studies show that observed fault planes have dip (to the north) angle range from 50° to 82°.

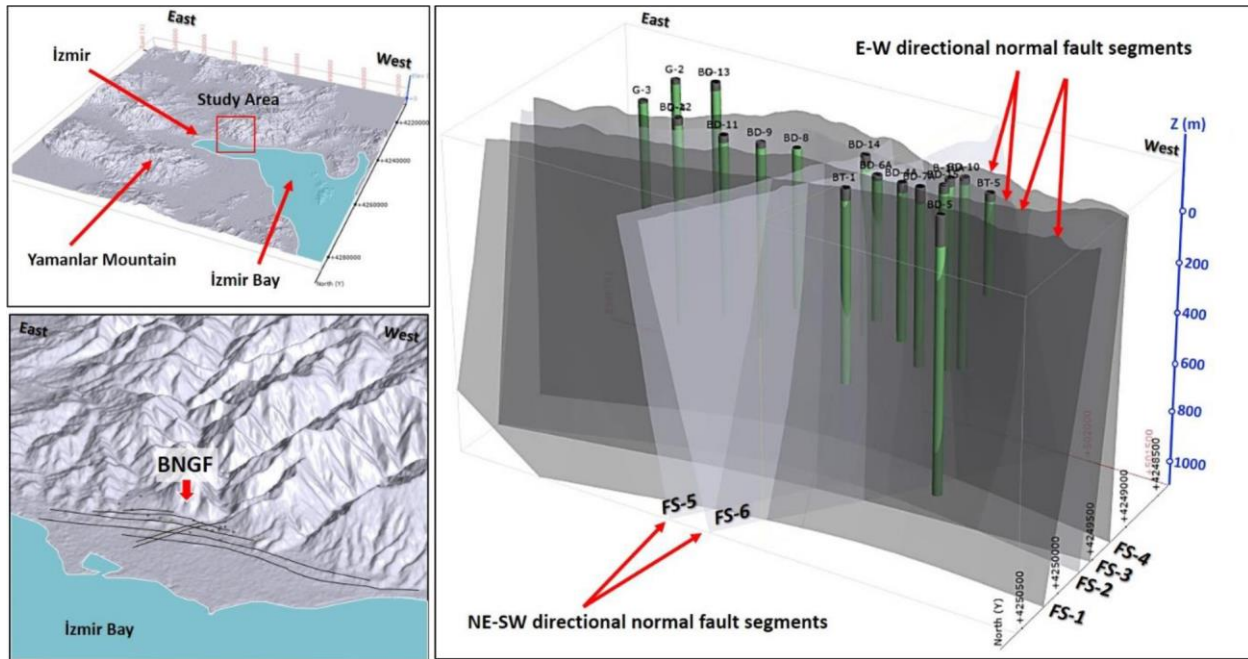


Figure 13. Fault segments demonstration of BNGF (Baba et al., 2022)

The meteoric geothermal water seep deep into rock of depth more than 2km via faults, joints and permeable zones in cases where they exist. After, the water is heated due to the heat of unknown source and rises up thanks to pressure difference and buoyance phenomenon. Then, water connects to fracture zone and segments and thus comes to the surface easily by means of the corridors along

the segments (Figure 14). The fluid runs to the north, where the alluvium formation has a connection to the sea, after arriving to the alluvium formation, which has some permeability and may easily convey flowing water. Considering that Bornova Complex is less porous and less permeable formation the hot water seeks for the paths supported by faults, joints, highly permeable fractures, which in turn, can be deduced as a secondary permeability. So, the connection of these permeable zones with the zones of intersection of normal fault planes and wellbores created extremely efficient flow pathways for the water to flow up to the surface. This results in avoiding of loss of heat of hot water due to fast movement of fluid. Furthermore, besides wells crossing only one segment such as wells G-2, BD-13 cutting FS-4 etc., there are wells crossing both E-W and NE-SW segments such as wells BT-1 and BD-5 cutting both FS-6 and FS-1 segment (Figure 13 and Figure 14).

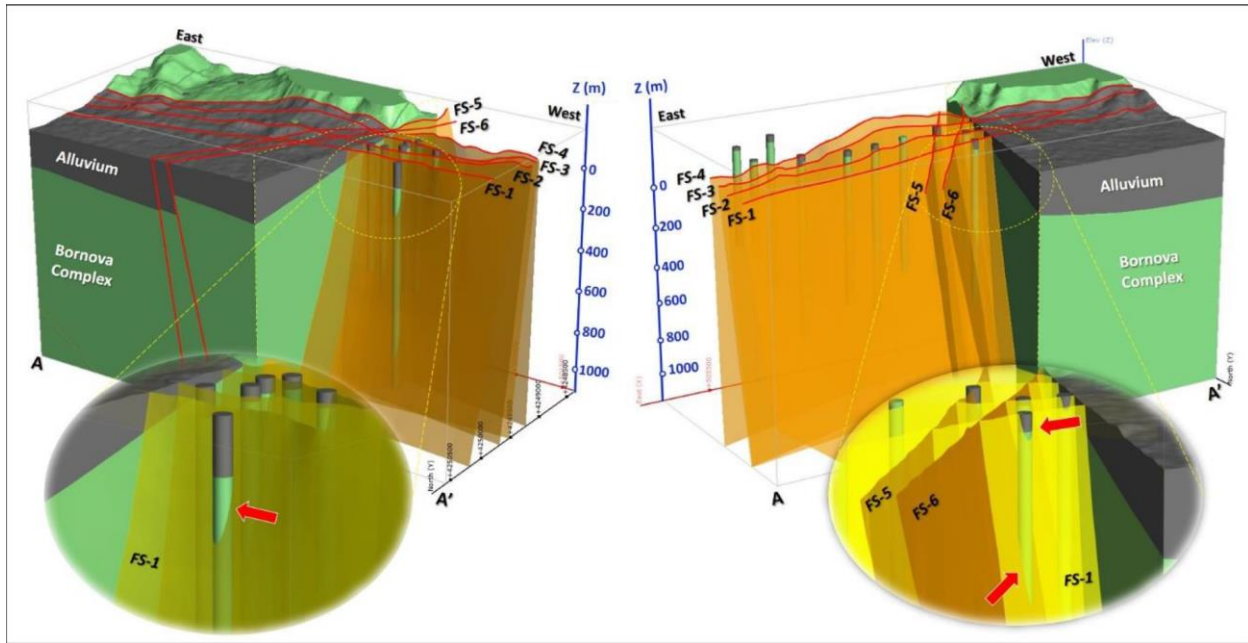


Figure 14. The pathways (thin red lines) through which geothermal water reaches the surface
(Baba et al., 2022)

2.4 Well properties in BNGF

Currently, in the Balçova geothermal field there are 26 wells opened by Izmir Geothermal Energy Company Inc., 11 of which are deep production wells, 5 wells are shallow production wells, 4 wells are re-injection wells, 4 wells are gradient wells for research goals and rest 2 wells are not feasible to use (Table 1). There was a renewal of six wells from 2013 to 2015. Besides these 26 wells, there are additional 11 wells drilled which belong to Izmir Governorship Investment Monitoring and Coordination Department.

Shallow wells are drilled to the depth below 200m, while deep wells reach the depths from 410 to 1000m (Figure 15). Maximum fluid temperature observed in the reservoir at well BD-11 is 140 °C, while minimum temperature observed is 60°C (Figure 16). Having noted that, looking at (Figure 16) distribution of geothermal wells in accordance with their temperature ranges (56-60, 60-80, 80-100, 100-120, 120-140) can be noticed.

Table 1. Wells and their characteristics in BNGF

<i>Well name</i>	<i>Year</i>	<i>Coordinates</i>		<i>Depth (m)</i>	<i>Temperature (°C)</i>	<i>Flow rate (l/s)</i>
		<i>X</i>	<i>Y</i>			
<i>Shallow production wells</i>						
B-10A	2013	4249023	502804	200	102	
B-1	1982	4248981	503124	104	102	100
B-4	1984	4248988	502959	125	100	60
B-5	1982	4248990	503077	108,5	102	140
B-7	1983	4249025	503179	120	96	140
<i>Deep production wells</i>						
BD-4A	2013	4249237	503056	613.45	128	
BD-6A	2013	4249220	503266	565	135	
BD-7A	2015	4249217	502925	700	105	
BD-1	1994	4249057	503002	564	110	60
BD-2	1995	4249211	503487	677	132	180
BD-5	1998	4249486	502608	1100	115	80
BD-9	2003	4249219	504216	772	138,5	360
BD-11	2007	4249245	504510	716	140	360
BD-12	2007	4249187	504943	830	137	300
BD-14	2007	4249040	503468	716	130	125
BD-15	2007	4249113	502798	472	105,6	
<i>Re-injection wells</i>						
BT-1	2014	4249500	503350	765		
BD-3	1996	4249204	503719	750		
BD-8	2002	4249211	503922	629		
BD-10	2004	4248985	502709	750		

<i>Gradient wells</i>						
G-1	2007	4248653	504963	413	70	
G-2	2006	4248664	505304	456	71,7	
G-3	2006	4249047	505328	435	70	
G-4	2006	4249187	504936	350	77,3	
<i>Unused wells</i>						
BD-13	2007	4248652	504963	720		
BT-6		4249080	503682			

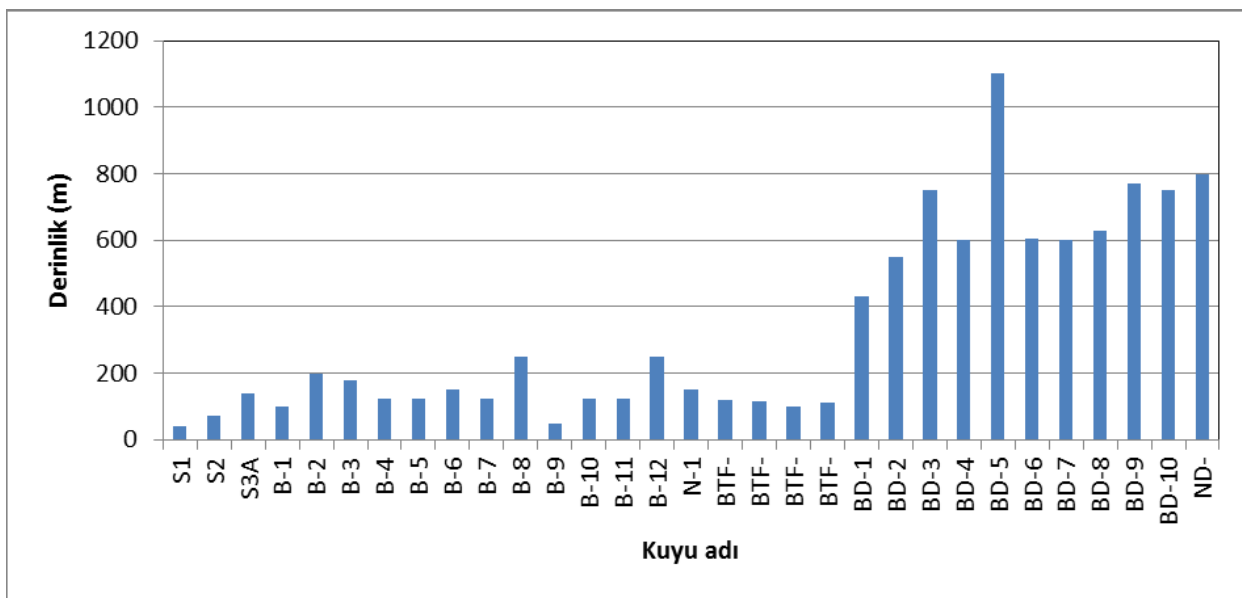


Figure 15. Depths of geothermal wells in BNGF

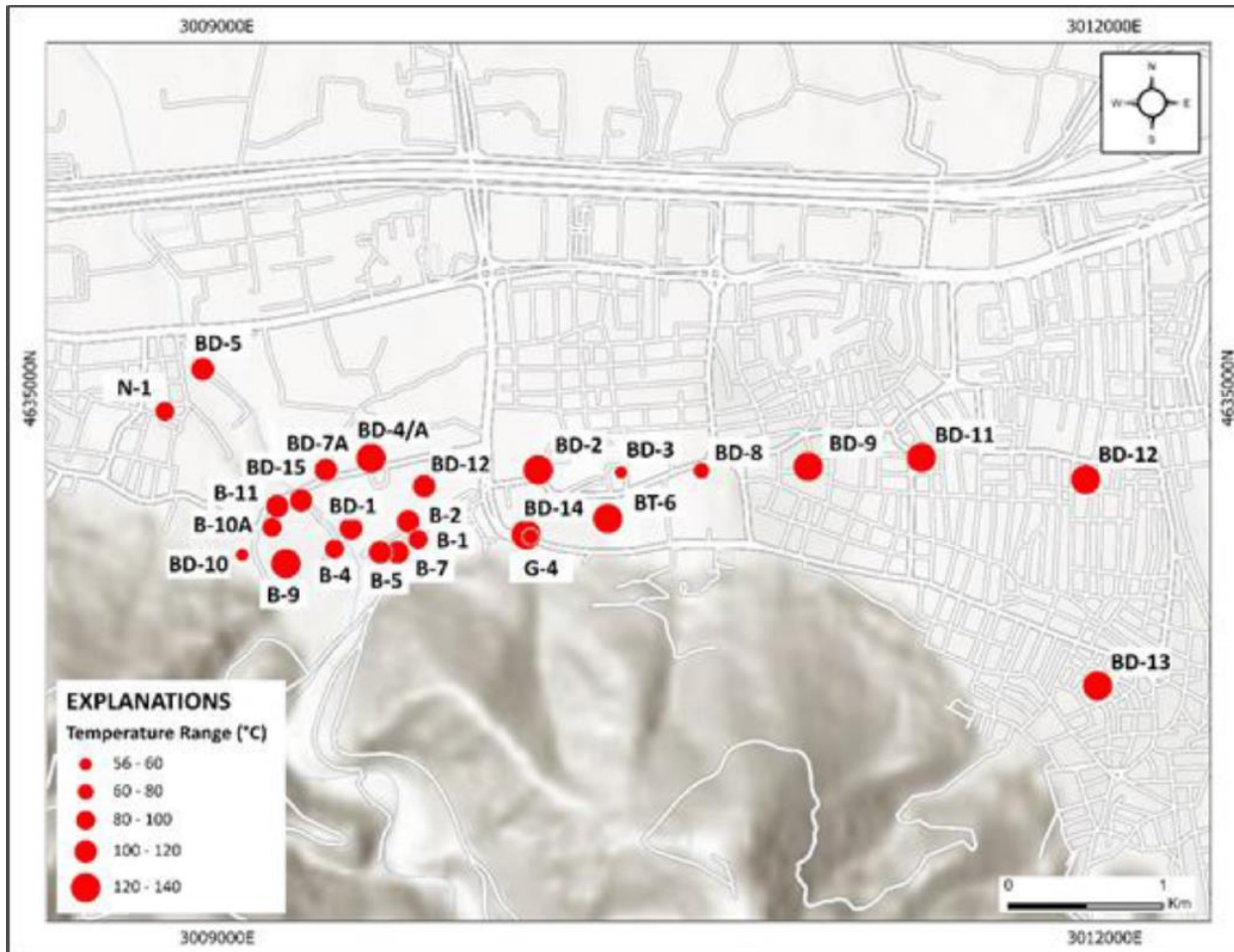


Figure 16. Temperature distribution in BNGF (Baba et al., 2022)

The information about lithological intervals corresponding to geothermal wells in BNGF have been derived from well logging data, which in turn, was performed by Izmir Geothermal Energy Company Inc. in the beginning years of field construction (Table 2). In the BD-5 well, which was drilled in 1998 and has a depth of 1100 m, there are clastics belonging to the 116 m alluvial unit and clastic units derived from flysch after 116 m. In the reinjection well BD-8, which was drilled in 2002 with a depth of 630 m, metasandstone, metasiltstone, meta claystone layers and partly quartzite-containing units belonging to the flysch unit were cut from the surface to the bottom of the well. In the BD-9 well, which was established in 2003 with a depth of 772 m, 0-18 m talus and units belonging to the Izmir flysch unit from 18 m to the bottom of the well were observed. In the BD-10 well, which is 750 m deep, 20 m of talus and then the units of the Izmir flysch unit were cut up to 750m. In the BD-11 (716 m deep) and BD-12 (830 m) wells drilled in 2006, 26m and 46m alluvial units were cut initially from surface, respectively, and then units belonging to the Izmir flysch unit till the bottomhole. Wells BD-6A and B-10A were drilled in 2013. According to the data of the B-10A well, 30 m thick alluvium-derived clastic units and metasandstone and meta

claystone-dominated flysch units between 30 m and 750 m depth were cut in the area. In the BD-6A well with a depth of 565 m, a 17 m thick alluvial unit was cut. After the alluvium unit, metasiltstone, metasandstone and meta claystone-dominated flysch unit was entered. In the shallow well B-4 drilled in 1984 with depth of 125m, alluvium dominated units from surface till 68m exist, then flysch-derived clastics are seen till the bottom of the well. The gradient well G-1 drilled in 2007, has a depth of 413 m and is comprised of talus-based formation of 30m thickness and after 30m flysch dominated units appear. Other 3 gradients wells G-2, G-3 and G-4 drilled in 2006, mainly has approximately 30m height alluvium based clastic units in the upper interval, while flysch derived units are in the lower interval after 30m.

Table 2. Lithological intervals crossed by geothermal wells

Well name	Year	Depth (m)	Formation	Well type
B-10A	2013	200	0-30 m Alluvium 30-200m Flysch	Shallow Production
B-4	1984	125	0-68m Alluvium 68-125m Flysch	Shallow Production
BD-4A	2013	613.45	0-35 m Alluvium 35-613.45 m Flysch	Deep Production
BD-6A	2013	565	0-17 m Alluvium 17-565 m Flysch	Deep Production
BD-2	1995	677	0-38 m Alluvium 38-677 m Flysch	Deep Production
BD-5	1998	1100	0-116 m alluvium 116-1100 m Flysch	Deep Production
BD-9	2003	772	0-18 m Talus 18-772 m Flysch	Deep Production
BD-11	2007	716	0-26 m Alluvium 26-716 m Flysch	Deep Production
BD-12	2007	830	0-46 m alluvium 46-830 m flysch	Deep Production
BD-14	2007	716	0-40 m Alluvium 40-371 m flysch	Deep Production
BD-15	2007	472	0-30 m Alluvium 30-472 m Flysch	Deep Production
BD-8	2002	629	0-629 m Flysch	Re-injection

BD-10	2004	750	0-20 m Talus 20-750 m Flysch	Re-injection
BD-13	2007	720	0-30 m Talus 30-720 Flysch	Out of use
G-1	2007	413	0-30 m Talus 30-413 m Flysch	Gradient
G-2	2006	456	0-14 m alluvium 12-456 m Flysch	Gradient
G-3	2006	435	0-7 m alluvium 5-435 m Flysch	Gradient
G-4	2006	350	0-27 m alluvium 27-350 m Flysch	Gradient

2.5 Hydrogeochemistry of geothermal fluid in BNGF

Geological, hydrogeological and geothermal studies in the Balçova-Narlıdere geothermal field have been continuing since 1960. In this study, Izmir Geothermal Energy Company Inc. took fluid samples for geothermal water analysis from production wells such as B-5A, B-10A, BD-4A, BD-6A, BD-9, BD-11, BD 5, BD 12, BD-14, B-1A and a re-injection well (BT-1) in 2022 January. Samples were also taken from different wells in 2022. pH, EC, alkalinity, major anion and cation, silicon and heavy metal (Al, As, B, Cr, Cu, Fe, Mn, Ni, S, Sr) analysis were made in the samples taken.

2.5.1 Physical properties of geothermal water

Production wells and re-injection well pH values in the geothermal field in 2020, 2021 and 2022 are shown in (Figure 18) and EC values are shown in (Figure 17).

The Electrical Conductivity (EC) values of the hot fluid in the deep production wells sampled in 2020 in the Balçova-Narlıdere geothermal field were 1852-1981 µS/cm; The EC value of the shallow production well is between 1803-1848 µS/cm and the EC values of the re-injection well are 1890 µS/cm. In the deep production wells sampled in 2021, the Electrical Conductivity (EC) values of the hot fluid are higher than previous year, 1930-2036 µS/cm; The EC value of the shallow production well is between 1814-1878 µS/cm and the EC values of the re-injection well are 1924 µS/cm. The Electrical Conductivity (EC) values of the hot fluid in the deep production wells sampled in 2022 are 1865-2115 µS/cm; The EC value of the shallow production well is between 1795-1917 µS/cm and the EC values of the re-injection well are 1966 µS/cm (Figure 17). In general, the EC values of the hot fluid are close to each other, indicating that the waters have similar properties. The highest EC values by years were measured in the BD-4A well, respectively.

EC values in deep wells are higher than shallow wells due to deep circulation and water-rock interaction. According to these data, the 2020 pH and EC values of the re-injection well are 7.32 and 1926 $\mu\text{S}/\text{cm}$, respectively, the 2021 pH and EC values are 6.87 and 1924 $\mu\text{S}/\text{cm}$, in 2022, the pH and EC values are 7.41 and 1966 $\mu\text{S}/\text{cm}$, respectively. It is observed that the values are in an average value compared to the production wells according to the years of sampling. The pH values of the hot fluid taken from the production wells vary between 6.42-8.07 in 2020, between 6.47-7.79 in 2021, and between 6.46-8.56 in 2022. Although the fluid of the BD-9 well showed acidic properties in every three years, it was observed that the fluid of the other wells was basic.

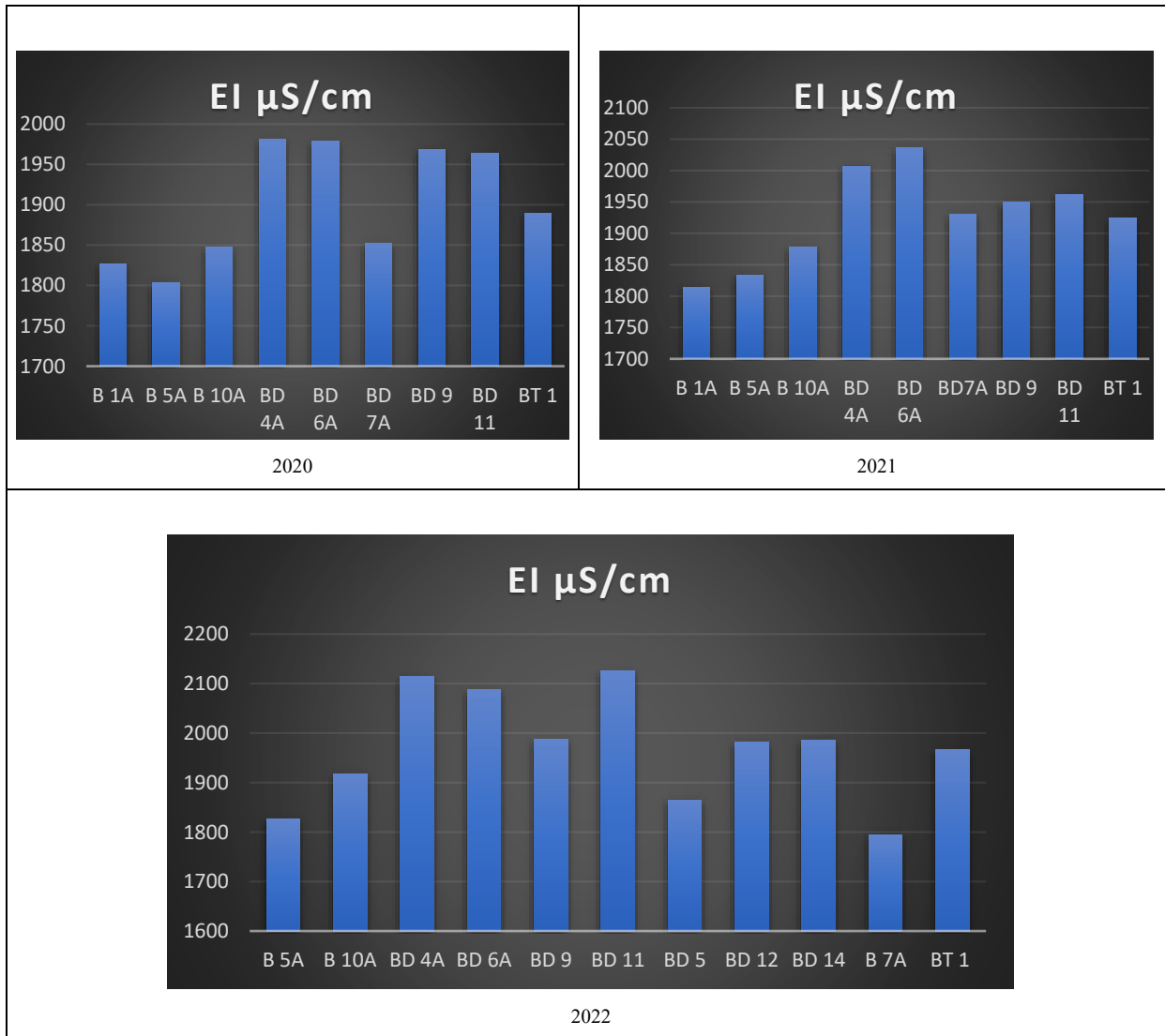


Figure 17. Electric Conductivity (EI) values derived from analysis of geothermal fluid sampled from production and re-injection wells in 2020, 2021, 2022.

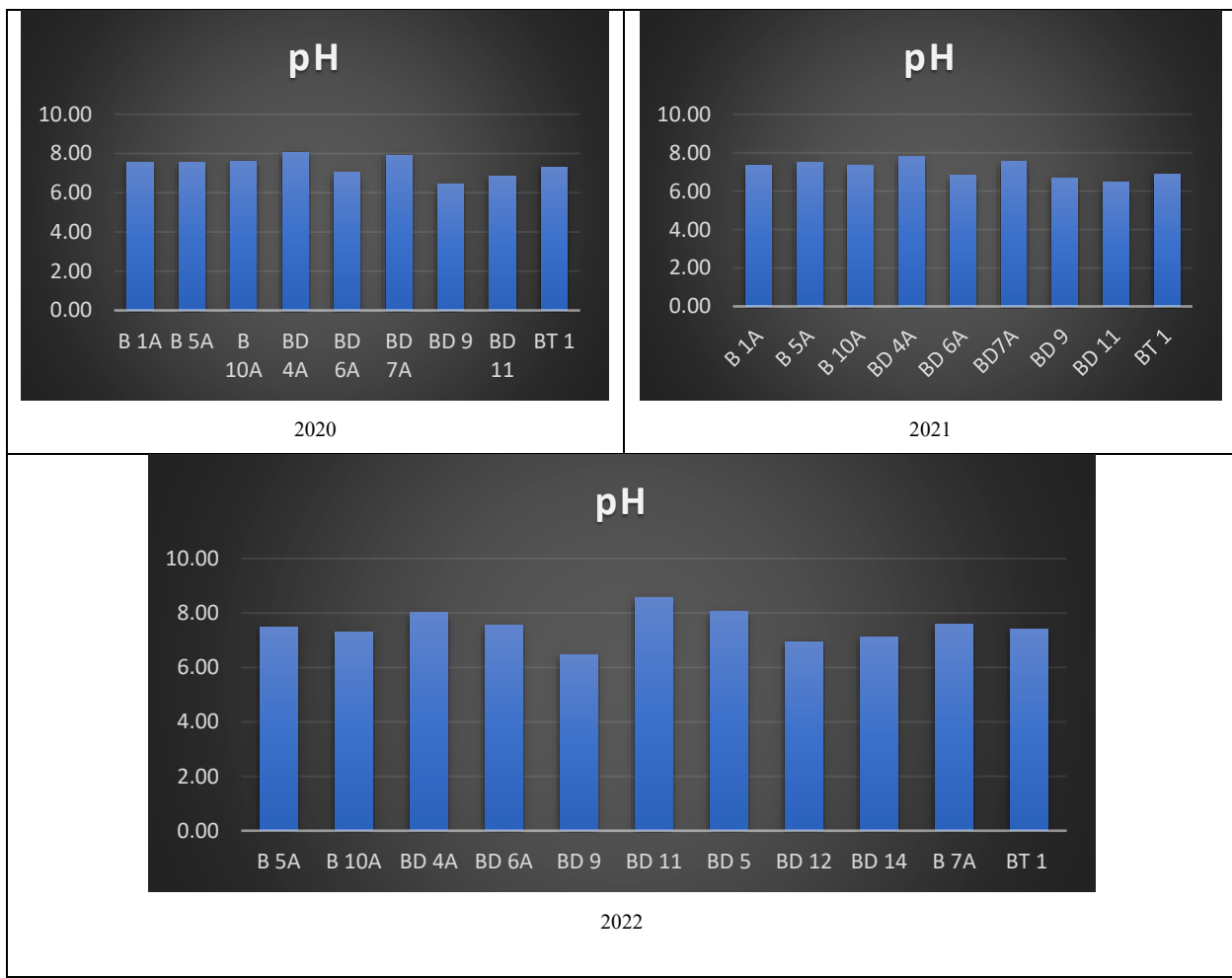


Figure 18. pH values derived from analysis of geothermal fluid sampled from production and re-injection wells in 2020, 2021, 2022.

2.5.2 Chemical properties of geothermal water

Major anion and cation analyses were performed to determine the origin relationships of the fluid in the Balçova-Narlıdere geothermal field (Table 3). Ca+2 concentrations in B-1A, B-5A, B-10A, BD-4A, BD-6A, BD-7A, BD-9 and BD-11 production wells where water samples were taken in 2020 were determined as 31.2, 24.5, 10.9, 18.8, 15.2 and 12.4 mg/L respectively, while Ca+2 concentrations were determined as 20.5 mg/L at BT-1 point which is a re-injection well, and Ca+2 concentrations in B-1A, B-5A, B-10A, BD-4A, BD-6A, BD-7A, BD-9 and BD-11 production wells where water samples were taken in 2021 were 25.8, respectively, While 29.7, 25.2, 15.5, 18.6, 19.1, 16.9 and 15.3 mg/L were determined, the concentrations of Ca+2 were determined as 21.1 mg/L at the re-injection well BT-1 point, in the 2022 water sample was B-5A, B-10A, BD-4A, BD-6A, BD-9, BD-11, BD-5, BD-12, BD-14 and B-7A production wells were determined as 30.9, 25.4, 16.4, 19.2, 21.7, 7.1, 13.8, 14.9 21.8 and 20.6 mg/L, respectively, while the re-injection

well was determined as 25.5 mg/L at the BT-1 point, respectively. Mg⁺² concentrations in 2020 were at the levels of 7.9, 10.3, 6.9, 2.1, 2.4, 5.3, 2.2 and 1.6 mg/L in B-1A, B-1A, B-5A, B-10A, BD-9 and BD-11 production wells, respectively, while 4.6 mg/L in re-injection well, and 8.9 in B-1A, B-5A, B-10A, BD-4A, BD-6A, BD-7A, BD-9 and BD-11 production wells in 2021 samples taken in 2021, respectively, Mg⁺² concentrations in the re-injection well were at the levels of 10.2, 6.6, 2.2, 2.8, 4.9, 2.1 and 1.2 mg/L, and in the samples taken in 2022, the concentrations of Mg⁺² were at the levels of B-5A, B-10A, BD-4A, BD-6A, BD-9, BD-11, BD-5, BD-12, BD-14 and B-7A were 3.9 mg/L in the re-injection well while at the levels of 10.9, 6.6, 2.2, 2.6, 1.9, 1.1, 2.1, 2.1, 4.3 and 7.2 mg/L respectively. In general, it is seen that Ca⁺² and Mg⁺² concentrations in shallow production wells are also higher than in deep production wells. Sodium concentration in groundwater can also be found at high levels due to factors such as water-rock interaction and/or seawater interference. In 2020, the Na⁺ concentrations determined at the production wells B-1A, B-5A, B-10A, BD-4A, BD-6A, BD-7A, BD-9 and BD-11 were 374, 374, 382, 439, 420, 529, 420 and 460 mg/L respectively, while the Na⁺ concentrations determined at the production wells B-1A, B-5A, B-10A, BD-4A, BD-6A, BD-7A, BD-9 and BD-11 in 2021 were 363, respectively, The Na⁺ concentrations determined at the production wells B-5A, B-10A, BD-4A, BD-6A, BD-9, BD-11, BD-5, BD-12, BD-14 and B-7A are 354, 384, 454, 446, 416, 465, 401, 420, 418 and 364 mg/L in the re-injection well while they are 359, 366, 425, 418, and 399 mg/L, respectively, at 359, 366, 465, 401, 420, 418 and 364 mg/L, respectively. As seen from the results of the analysis of the three years, it was determined that the Na⁺ concentrations at the shallow production wells B-1A, B-5A, B-7A and B-10A points were lower than the deep production wells BD-4A, BD-5A, BD-6A, BD-7A, BD-9, BD-11, BD-12 and BD-14. Due to the deep circulation of fluid and water-rock interaction in deep wells, the concentration of Na⁺ has reached higher concentrations. In 2020, the K⁺ concentrations determined in the samples taken from the B-1A, B-5A, B-10A, BD-4A, BD-6A, BD-7A, BD-9 and BD-11 production wells were determined to be at the levels of 28.2, 27.1, 27.7, 31.2, 30.7, 29.1, 32.8 and 33.3 mg/L, respectively, while the K⁺ concentrations determined in the re-injection well were 29.6 mg/L, and in 2021, the K⁺ concentrations determined in the samples taken from the B-1A, B-5A, B-10A, BD-4A, BD-6A, BD-7A, BD-9 and BD-11 production wells were 27.1, respectively, The K⁺ concentrations determined in the samples taken from the production wells 26.6, 30.6, 30.7, 26.3, 31.6, and 32.4 mg/L were determined to be 27.9 mg/L, in 2022 the K⁺ concentrations determined in the samples taken from the B-5A, B-10A, BD-4A, BD-6A, BD-9, BD-11, BD-5, BD-12, BD-14 and B-7A production wells were 24.9, 27.1, 31.1, 35.9, 28.8, 32.2, 30.7, and 27.4 mg/L, respectively, while the K⁺ concentration determined in the re-injection well was 28.3 mg/L. As with sodium values, K⁺ values are slightly higher in deep production wells. In 2020, the SO₄⁻² concentrations determined at the points B-1A, B-5A, B-10A, BD-4A, BD-6A, BD-7A, BD-9 and BD-11 were 159, 159, 163, 171, 163, 161, 164 and 164 mg/L, respectively, while the SO₄⁻² concentrations determined at the production wells B-1A, B-

5A, B-10A, BD-4A, BD-6A, BD-7A, BD-9 and BD-11 points in 2021 were 160 respectively, The SO₄⁻² concentrations determined at the points 163, 158, 171, 170, 164, 168 and 165 mg/L in the re-injection well, and 162 mg/L in the re-injection well, while the SO₄⁻² concentrations determined at the B-5A, B-10A, BD-4A, BD-6A, BD-9, BD-11, BD-5, BD-12, BD-14 and B-7A points are 161, 165, 182, 178, 172, 178, 188, 172, 170, 170 and 162 mg/L in the production wells in 2022, respectively. 2020, 2021 and 2020

Table 3. Major anion-cation measurements at the sampling points determined in the Balçova geothermal area

2020														
Örnek Adı	Ca ⁺² (mg/L)	Mg ⁺² (mg/L)	Na ⁺ (mg/L)	K ⁺ (mg/L)	SO ₄ ⁻² (mg/L)	CO ₃ ⁻² (mg/L)	HCO ₃ ⁻ (mg/L)	Cl ⁻ (mg/L)	Li ⁺ (mg/L)	NH ₄ ⁺ (mg/L)	F ⁻ (mg/L)	NO ₂ ⁻ (mg/L)	Br ⁻ (mg/L)	NO ₃ ⁻ (mg/L)
B-1A	25,882	7,940	374,716	28,278	159,97	---	733	184,20	1,291	1,508	7,26	---	0,32	0,13
B-5A	29,774	10,397	374,976	27,069	159,04	---	709	182,29	1,244	1,437	6,76	---	0,31	0,08
B-10A	25,213	6,938	382,036	27,759	163,07	---	702	188,30	1,294	1,408	7,59	---	0,31	<0,05
BD-4A	15,550	2,136	439,218	31,244	171,80	---	750	199,61	1,492	1,295	7,97	---	0,35	0,10
BD-6A	18,616	2,459	420,988	30,756	163,76	---	801	192,77	1,476	1,583	7,49	---	0,34	0,09
BD-7A	19,161	5,392	529,118	29,057	161,75	---	700	184,45	1,366	1,409	7,49	---	0,33	0,27
BD-9	16,952	2,272	420,408	32,848	164,84	---	756	207,96	1,480	1,775	7,95	---	0,36	0,08
BD-11	15,341	1,676	460,298	33,302	164,55	---	700	209,78	1,491	1,794	7,94	---	0,37	<0,05
BT-1	21,160	4,670	398,008	29,698	161,36	---	707	189,39	1,387	1,576	7,32	---	0,36	0,09

2021														
Örnek Adı	Ca ⁺² (mg/L)	Mg ⁺² (mg/L)	Na ⁺ (mg/L)	K ⁺ (mg/L)	SO ₄ ⁻² (mg/L)	CO ₃ ⁻² (mg/L)	HCO ₃ ⁻ (mg/L)	Cl ⁻ (mg/L)	Li ⁺ (mg/L)	NH ₄ ⁺ (mg/L)	F ⁻ (mg/L)	NO ₂ ⁻ (mg/L)	Br ⁻ (mg/L)	NO ₃ ⁻ (mg/L)
B-1A	30,215	8,953	363,850	27,041	160,85	---	679	188,37	1,220	1,518	7,34	---	0,32	0,06
B-5A	34,481	10,226	359,605	26,664	163,60	---	692	191,24	1,218	1,442	7,15	---	0,32	0,07
B-10A	24,283	6,681	366,370	26,276	158,25	---	708	185,87	1,265	1,473	7,39	---	0,31	0,08
BD-4A	18,135	2,235	425,778	30,622	171,79	---	766	203,22	1,440	1,416	8,22	---	0,34	0,03
BD-6A	22,167	2,816	418,356	30,799	170,42	---	784	204,69	1,451	1,662	7,89	---	0,35	0,07
BD-7A	19,916	4,932	389,370	26,346	164,59	---	697	192,44	1,373	1,514	7,94	---	0,33	0,05
BD-9	16,853	2,142	398,486	31,647	168,89	---	703	209,17	1,407	1,829	8,18	---	0,36	0,08
BD-11	14,491	1,252	399,470	32,420	165,88	---	689	212,83	1,435	1,873	8,28	---	0,37	0,05
BT-1	21,100	4,930	388,306	27,912	162,40	---	737	184,64	1,331	1,584	6,73	---	0,33	0,37

2022														
Örnek Adı	Ca ⁺² (mg/L)	Mg ⁺² (mg/L)	Na ⁺ (mg/L)	K ⁺ (mg/L)	SO ₄ ⁻² (mg/L)	CO ₃ ⁻² (mg/L)	HCO ₃ ⁻ (mg/L)	Cl ⁻ (mg/L)	Li ⁺ (mg/L)	NH ₄ ⁺ (mg/L)	F ⁻ (mg/L)	NO ₂ ⁻ (mg/L)	Br ⁻ (mg/L)	NO ₃ ⁻ (mg/L)
B 5A	30,940	10,952	354,312	24,946	161,50	---	616	187,41	1,223	1,434	7,50	---	0,32	0,05
B 10A	25,460	6,686	384,806	27,124	165,13	---	653	193,73	1,323	1,543	7,80	---	0,33	0,06
BD 4A	16,420	2,227	454,384	31,108	182,91	---	729	212,40	1,510	1,454	8,32	---	0,38	0,10
BD 6A	19,295	2,634	446,536	30,640	178,37	---	778	213,29	1,512	1,614	8,75	---	0,37	0,08
BD 9	21,763	1,966	416,790	31,418	172,75	---	680	218,47	1,468	1,811	8,80	---	0,38	<0,05*
BD 11	7,120	1,178	465,070	35,990	188,13	---	540	241,40	1,616	1,296	9,99	---	0,42	0,15
BD 5	13,883	2,074	401,636	28,846	172,79	---	628	204,51	1,356	1,612	9,47	---	0,35	0,14
BD 12	14,913	2,030	420,960	32,266	170,07	---	664	222,52	1,495	1,849	8,92	---	0,39	<0,05*

BD 14	21,883	4,014	418,284	30,772	170,19	---	714	210,82	1,463	1,728	8,39	---	0,37	<0,05*
B 7A	25,503	7,265	364,706	27,452	162,04	---	636	188,62	1,274	1,605	7,68	---	0,32	0,10
BT 1	20,676	3,918	404,580	28,312	167,88	---	689	198,96	1,396	1,649	8,14	---	0,34	0,21

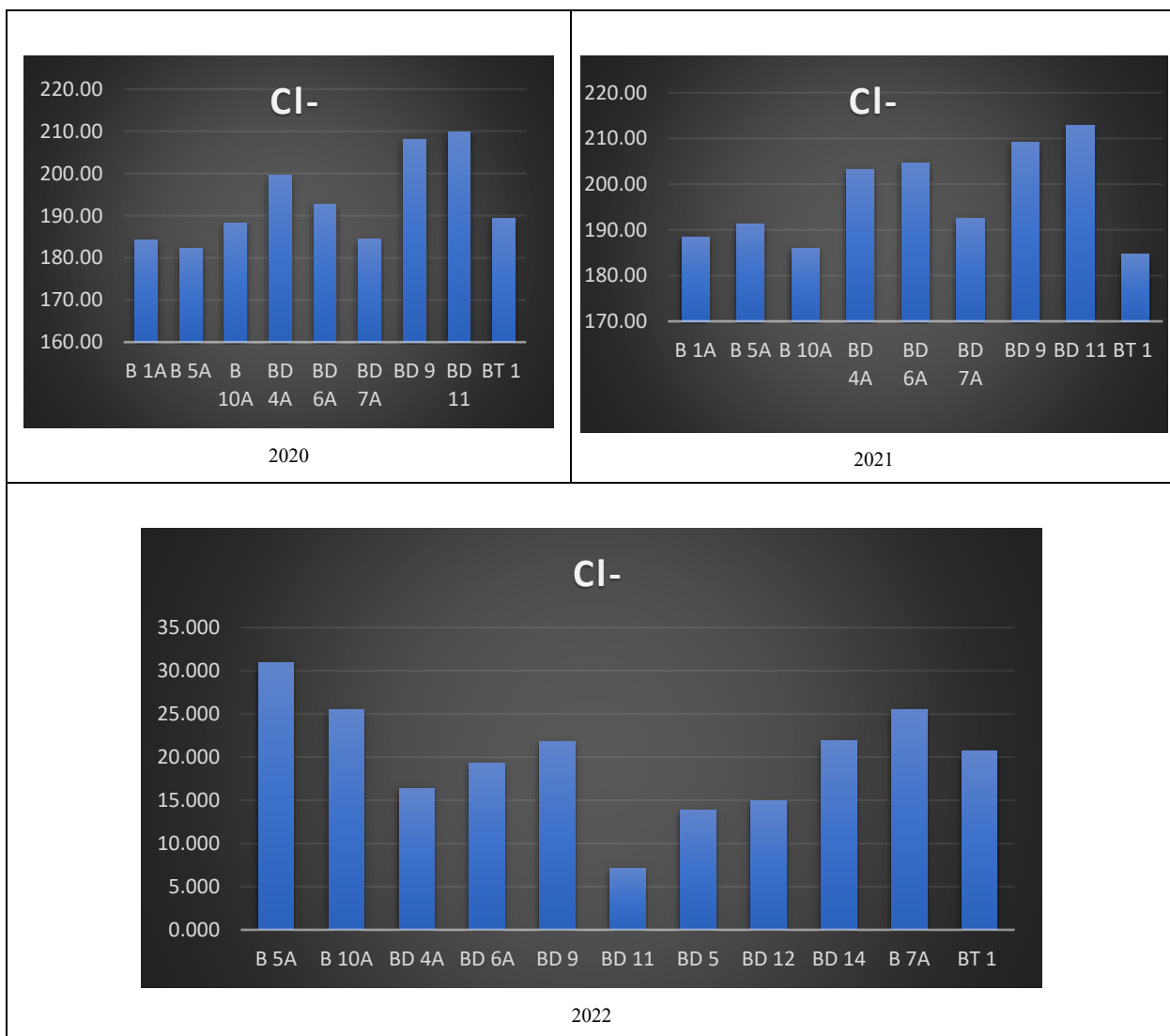


Figure 19. Cl⁻ values of production wells and re-injection wells in the Balçova-Narlıdere geothermal field

- The pH values of the hot fluid in the deep production wells in the Balçova-Narlıdere geothermal area vary between 6.42-8.07 in 2020, between 6.47-7.79 in 2021, and between 6.46-8.56 in 2022. Although the fluid of the BD-9 well showed acidic properties in every three years, it was observed that the fluid of the other wells was basic.
- In general, it is seen that Ca²⁺ and Mg²⁺ concentrations in shallow production wells are higher than in deep production wells.
- It is dominated by fluid Na⁺ and HCO₃⁻ ions in both shallow and deep production wells.

- According to the Schoeller diagram, while the dominant cation in the hot fluid in the geothermal field is Na+K, the dominant anion is HCO₃²⁻ and these waters are Na-HCO₃ waters. As a result of the hydrogeochemical evaluations made in the study area, it has been determined that the dominant ion sequence of the hot waters is Na+K>Ca>Mg and HCO₃>Cl>SO₄.
- According to the Piper diagram, the fact that the hot fluid is located in the same region shows that they are of the same origin and have a similar circulation path.
- Boron (B) values vary between 10.6-13.8 mg/L in 2020, 8.9-13.1 mg/L in 2021, and 8.3-12.9 in 2022.

CHAPTER 3: PROBLEM STATEMENT

Since past decades demand for one of the renewable energy sources, geothermal energy has been increasing significantly. Therefore, the amount of produced and re-injected geothermal fluid has been enhanced to a substantial degree in order to provide more environmentally sustainable energy to people, units. All contemporary, sustainable, and eco-friendly geothermal utilization projects entail geothermal reinjection, which involves reintroducing fluid that has lost energy into geothermal systems. It is an effective way to recharge geothermal systems in addition to being an efficient way to dispose of wastewater. As a result, it boosts production capacity in most circumstances, reduces production-induced pressure drawdown, and draws more heat energy from reservoirs.

Considering that geothermal source reserves in Izmir are in high amounts, the production and re-injection processes should be carried out in quite careful way to avoid any possible damages that could be done to the geothermal reservoir and its characteristics such as permeability, porosity etc. Damages can bring consequences such as an early decrease in reservoir pressure because of fast high production but insufficient injection. Other important outcomes can be fast reservoir temperature decline from excessive injection amount and early breakthrough.

Although the field has the potential for further development, it is important to carefully examine the field's reaction to the anticipated rise in the amounts of produced and injected geothermal water to determine any potential impacts. The most popular method for researching such issues is modeling research using reservoir simulation software. Numerical simulation is implemented and natural state modelling, history matching and various scenarios to estimate the performance of the field and make a forecast, are achieved by means of TOUGH2 software designated for multiphase and multicomponent fluid flow.

CHAPTER 4: METHODOLOGY

The reservoir simulation analyzes the behavior of reservoirs using the ideas and methods of mathematical modeling. Reservoir simulation can refer to the entire system, that encompasses the reservoir, the surface equipment, as well as any interconnected major activity. However, in narrower sense, it simply relates flow hydrodynamics in the reservoir. Every reservoir simulation research contains a number of procedures that allow different model component characteristics to be changed as necessary to match the measured and estimated data. The conceptual model serves as the foundation for model elements including permeability distribution, boundary conditions and fluid and heat sources. In that regard, the necessary data is collected and verified. The reservoir simulation is performed by the following major steps:

- Grid model construction. Certain rock properties such as porosity, permeability, production/injection values, heat conductivity are assigned to each grid block within the model.
- Natural state modelling where initial pressure and temperature distribution should be identified. Then the data obtained via model should be matched to actual measured data.
- History matching. Here model outcome is compared to actual data and any necessary changes are carried out to obtain better match.
- Forecasting. Here future predictions are made under the conditions of various production/injection scenarios in order to estimate field future performance.

Almost all the basic processes to perform the steps of reservoir simulation are implemented using TOUGH2 software along with the data obtained from Izmir Geothermal Energy Company Inc.

4.1 TOUGH2 software

TOUGH2 is a numerical simulation software designated for multi-dimensional fluid and heat flows of multiphase, multicomponent fluid mixtures in porous and fractured media. Various fluid mixtures can be managed with TOUGH2 software, and each one's characteristics are covered in its own Equation-of-State (EOS) module. TOUGH2 employs first-order fully implicit time differencing as well as an integral finite difference approach for space discretization. For solving linear equations, one can choose from a number of preconditioned conjugate gradient techniques or a sparse direct solver. Equations from the steam table accurately capture the thermophysical characteristics of water. The program offers choices for specifying heat and fluid injection or withdrawal. There are approaches for modeling fluid flow in fractured porous media, including multiple interacting continua (MINC) technique, dual-permeability and double-porosity approaches (*TOUGH2 / PetroMehras Directory*, n.d.).

TOUGH2 can be used to solve a broad range of issues with heat and moisture transmission, as well as the drying of porous materials, while being designed mainly for geothermal reservoir research and high-level nuclear waste isolation. Strongly heat-driven flow issues are the focus of the TOUGH2 simulator. TOUGH2 considers fluid flow that occurs under pressure, viscosity, and

gravitational forces in compliance with Darcy's Law in both the liquid and gaseous phases. Relative permeability functions are used to illustrate the interaction between the phases. (*TOUGH2 / PetroMehras Directory*, n.d.)

4.2 Modules of Equation of State

Equation-of-state (EOS) modules offer the thermophysical characteristics of fluid mixtures necessary for putting together the governing mass- and energy-balance equations. The EOS module should also perform the following three tasks (PRUESS et al., 1996):

- Provided set of main variables' phase conditions must be identified (element by element)
- Phase appearance and disappearance must be recognized as a main variable alteration while conducting Newton-Raphson iteration procedure
- Main variable should be switched when phase changes

4.2.1 EOS 1

EOS1 module is the most fundamental one. It describes pure water in its vapor, liquid and two-phase states and can represent two fluids with the same physical characteristics but different trace element contents. For single phase conditions, the main variables are pressure and temperature. Gas pressure-gas saturation or temperature-gas saturation are employed as the main variables for two-phase circumstances. If two waters with different trace elements and the same physical characteristics are to be employed, the third main variable, X, which is the mass fraction of water 2, is used.

4.2.2 EOS 2

This module is established in 1985 in order to handle fluids in geothermal reservoirs with high amount of gases, especially CO₂ rich fluids, in which its mass fraction ranges up to 80 percent or more. It takes into account heat-of-solution impacts and non-ideal behavior of gaseous CO₂ and CO dissolution in the aqueous phase as described by Henry's law. For single phase conditions, primary variables are temperature, pressure and CO₂ partial pressure, while for two-phase conditions, they are gas saturation phase pressure, gas saturation, and CO₂ partial pressure.

4.2.3 EOS 3

The EOS3 can handle both air and water. The behavior of air is believed to be that of an ideal gas. To get gas phase pressure, the vapor and air partial pressures are summed. Henry's constant is maintained constant because the variation with temperature is so negligibly small. For a single-phase condition, the main variables are air mass fraction, pressure and temperature for gas phase conditions. Gas saturation is added by 10 to distinguish between single- and two-phase circumstances.

4.2.4 EOS 4

Air, water, and the capacity to lower vapor pressure can all be handled by EOS4. In addition to temperature, capillary pressure, that is a function of saturation, also affects vapor pressure. For

single-phase conditions, the most important variables are air partial pressure, pressure and temperature; for two-phase conditions, they are gas saturation, gas phase pressure and air partial pressure.

EOS1 is chosen to be employed in the program because geothermal water in the BNGF has low content of non-condensable CO₂, which is about 0.08 percent in weight).

4.2.5 EOS 5

This module was created to investigate the geothermal water behavior that are experiencing hydrogen emission. The fundamental distinction from EOS3 is that hydrogen, which has differing thermophysical properties, replaces the air component. Similar to EOS3, EOS5 handles and assigns the same primary thermodynamic variables.

4.3 Petrasim

It is used as a graphical user interface for the whole simulator family of TOUGH2. By allowing the analyst to concentrate on the model while automatically taking care of the intricate details of TOUGH2 files, Petrasim greatly decreases the barriers to TOUGH2 adoption (*PetraSim - RockWare*, 2022). It guides the user in the following aspects:

- Equation of State choice
- Choosing which general options to apply to the analysis.
- Outlining the material's characteristics
- Defining cell-specific data, like sources, starting conditions, sinks and material, utilizing the grid editor.
- Choosing the output option and solution.
- Handling the problem.
- The data post-processing by means of time history and contour plots

4.4 Model construction

The enthalpy of 6.6×10^6 J/kg and temperature of 140°C of hot water have been defined and introduced to model. There are 45696 total blocks in the grid model. There are 42 blocks in the x direction, 32 blocks in the y direction, and 34 blocks in the z direction. 4.89 km² are covered by the surface. The system has dimensions of 3200 m, 1600 m, and 2550 m in the x, y, and z axes, respectively. Thus, the overall volume is close to 13km³. The blocks are 10 m thick from the surface to a depth of 100 m. These thin thicknesses allow for the separation of various formations, permeable zones, and impermeable zones at almost precise depths, allowing for the representation of fault throws in the model. Blocks in deeper parts have thicker walls than those in shallower sections.

In the model, thin columns 5 m wide are used to depict the 2000 md AG-I fault, which is referred to as a material Fault (Table 4). In cells close to the AG-I fault, the material Rock2 with a

permeability of 100mD was assigned. Alluvium formation near to the surface is connected to the AG-I fault. The element Rock2 is used in the model to depict the creation of alluvium. The permeability of the western portion of the AG-I fault must have been set higher than that of the rest of the fault in order to make the computed temperature values match the actual temperature readings. The material of the western part of Fault1 is named Fault2 and owns permeability of 6000mD. Rock3 formation is assigned as northern section of Fault2 and it has a permeability of 300mD. Rock1 is referred to the remaining part of the field. Air and Air2 are assigned as an air in the surface at temperature of nearly 20°C. All the characteristics for both air terms are the same except heat conductivity which is the main reason to distinguish them. All the values of density, specific heat and heat conductivity are average default values used in software. Other porosity, permeability and density value of formations are taken from the literature and field data set.

Table 4. Material properties within the model

Material name	Porosity	Permeability (m^2)			Denisty (kg/m^3)	Heat conuddctivity ($\text{W}/\text{m}^*\text{C}$)	Specific heat ($\text{J}/\text{kg}^*\text{C}$)
		K_x	K_y	K_z			
Fault (AG-I)	0.1	2×10^{-12}	2×10^{-12}	2×10^{-12}	2600	2	1000
Fault2	0.1	6×10^{-12}	6×10^{-12}	6×10^{-12}	2600	2	1000
Rock1	0.03	0	0	0	2600	2	1000
Rock2	0.1	10^{-13}	10^{-13}	10^{-13}	2600	2	1000
Rock3	0.1	3×10^{-13}	3×10^{-13}	3×10^{-13}	2600	2	1000
Air (20°C)	0	0	0	0	1.2	0.3	1000
Air2	0	0	0	0	1.2	0.1	1000

4.5 Natural state modelling

The stage of modeling geothermal reservoirs known as "natural state modeling" simulates the condition of the field prior to its exploitation. Geothermal reservoirs are known to change over geological time. In comparison to changes brought about by the exploitation of a reservoir, the rate of change of thermodynamic characteristics during natural state is negligible. This leads to the conclusion that pseudo-steady state conditions can be applied to geothermal reservoirs in the natural state. In order to achieve the pseudo-steady state, it is standard procedure in the simulation of geothermal reservoir to conduct the model without any kind of production/injection conditions. Trial and error techniques were used to develop the natural state model until the calculated and measured temperatures were reasonably in agreement.

The boundary conditions considered in natural state modelling of BNGF are as follows:

- The mass flow rate and enthalpy of the hot water flowing to the reservoir are 50kg/s and $6.6 \times 10^5 \text{ J/kg}$.

- There is no-flow boundary condition in terms of heat and fluid flow between the model and the area around the model.
- The hot water enters the reservoir from east of the AG-I fault at the point 1500m deep from surface and 1140m away from that depth in x direction.
- The hydrostatic pressure in the northern section of alluvium formation is about 5bar.

4.6 History matching

History matching has been carried out using pressure and temperature data obtained from natural state modelling and injection and production data recorded for 15 years from the start of exploitation of the BNGF in the correspondence with the data consistency. The results of history match from 1996 till 2010 have been demonstrated later in research.

4.7 Forecasting

The future reservoir performance predictions have been made after process of doing calibrations and analysis of history matching. The predictions have been made by estimating three various scenarios where production and injection rates have been changed.

- In the Scenario-I, the production and injection flow rates have been kept same for next 20 years beginning from 2008. As the history matching end data corresponds to year 2008, it has been chosen as an initial state where the simulation scenario starts. It is significant to note that, in 2008, 80 percent of all injections were made through the BD-8 well. The rest of injection was done mainly through wells BD-10 and BD-3. In this scenario, there are also wells which are used both for production and injection purposes such as BD-5, BD-1, BD-15. However, they were used as production wells only beginning from 2009. In the later field life, well BT-1 has been utilized as an injection well, too.

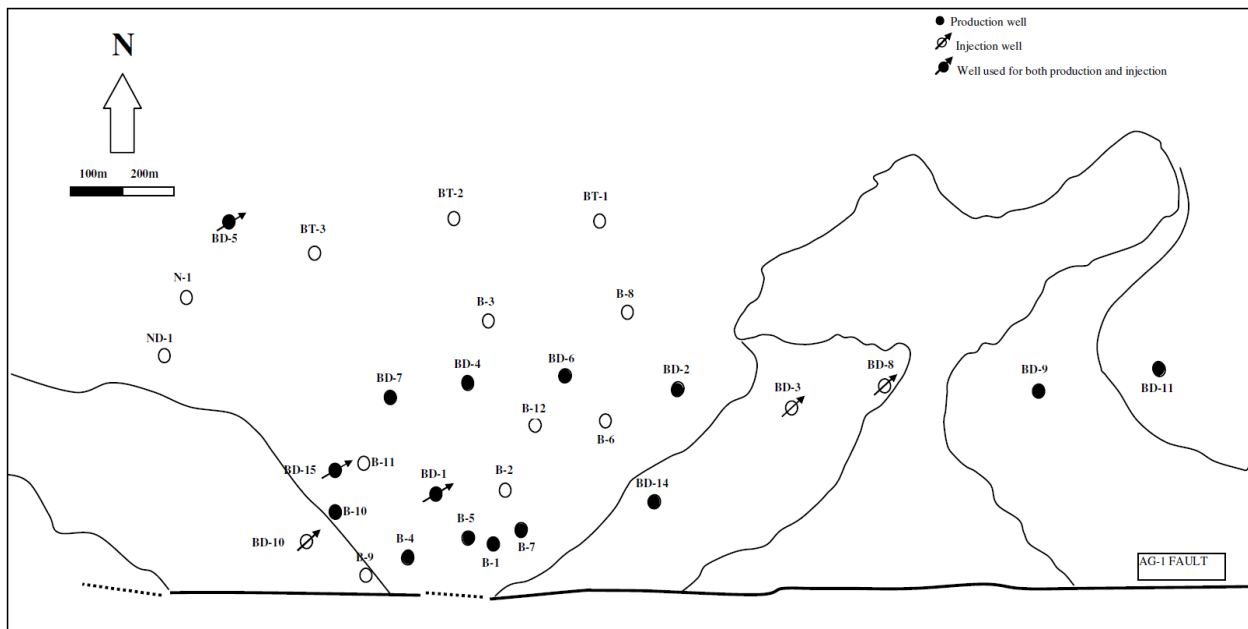


Figure 20. Production/injection well scheme for Scenario-I

- In Scenario-II, the simulation has been carried out for 15 years' period. Initially, the production and injection rates remain the same for first three years, after which they have been increased by 10% and 17%, respectively, every three years. In order to avoid pressure reduction issues as production rises, the injection to production ratio had to be raised. Later, more water will need to be injected later than what is generated and this is improbable in practice. In comparison with the Scenario-I, in this scenario, wells BD-5, BD-1 and BD-15 are used only for production and the other three injection wells are the same as in the first scenario.

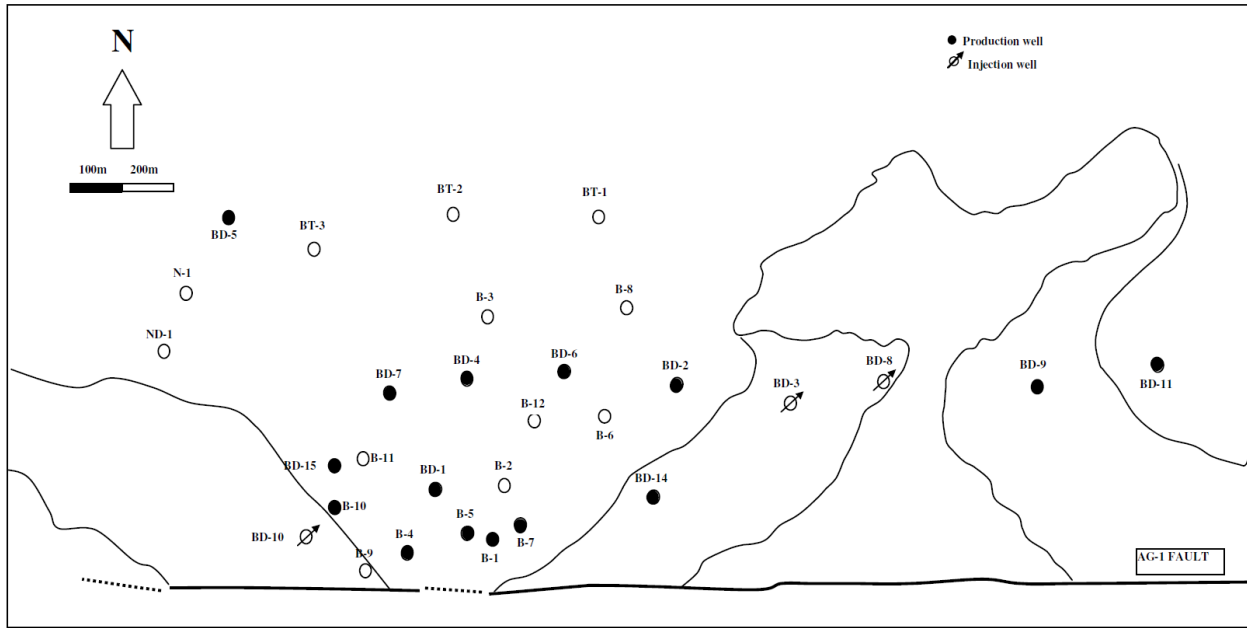


Figure 21. Production/injection well scheme for Scenario-II

- Scenario-III includes new BT-1 well drilled at depth of 765m to operate as an injection well from start of simulation. Here, about 60 percent of injected water through well BD-8 have been transferred to newly operating well BT-1. Scenario-III has the same production scenario as in Scenario-II. The production flow rate has been enhanced by 10 percent for each three years, after first three years of simulation start. Injection scenario is different from previous scenario. After first three years, the flow rates of injected fluid through wells BD-8, BD-3 and BD-10 have been raised by 25percent for every next 3 years for 15 years period run. However, the flow rate of well BT-1 has not been changed throughout the simulation period.

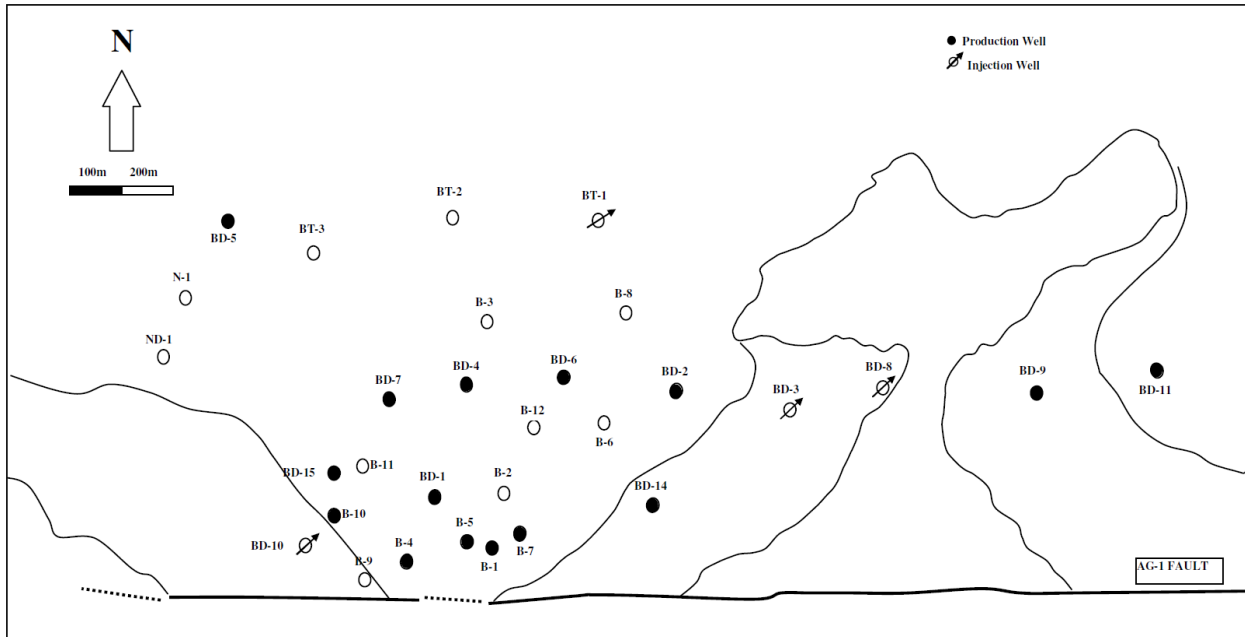
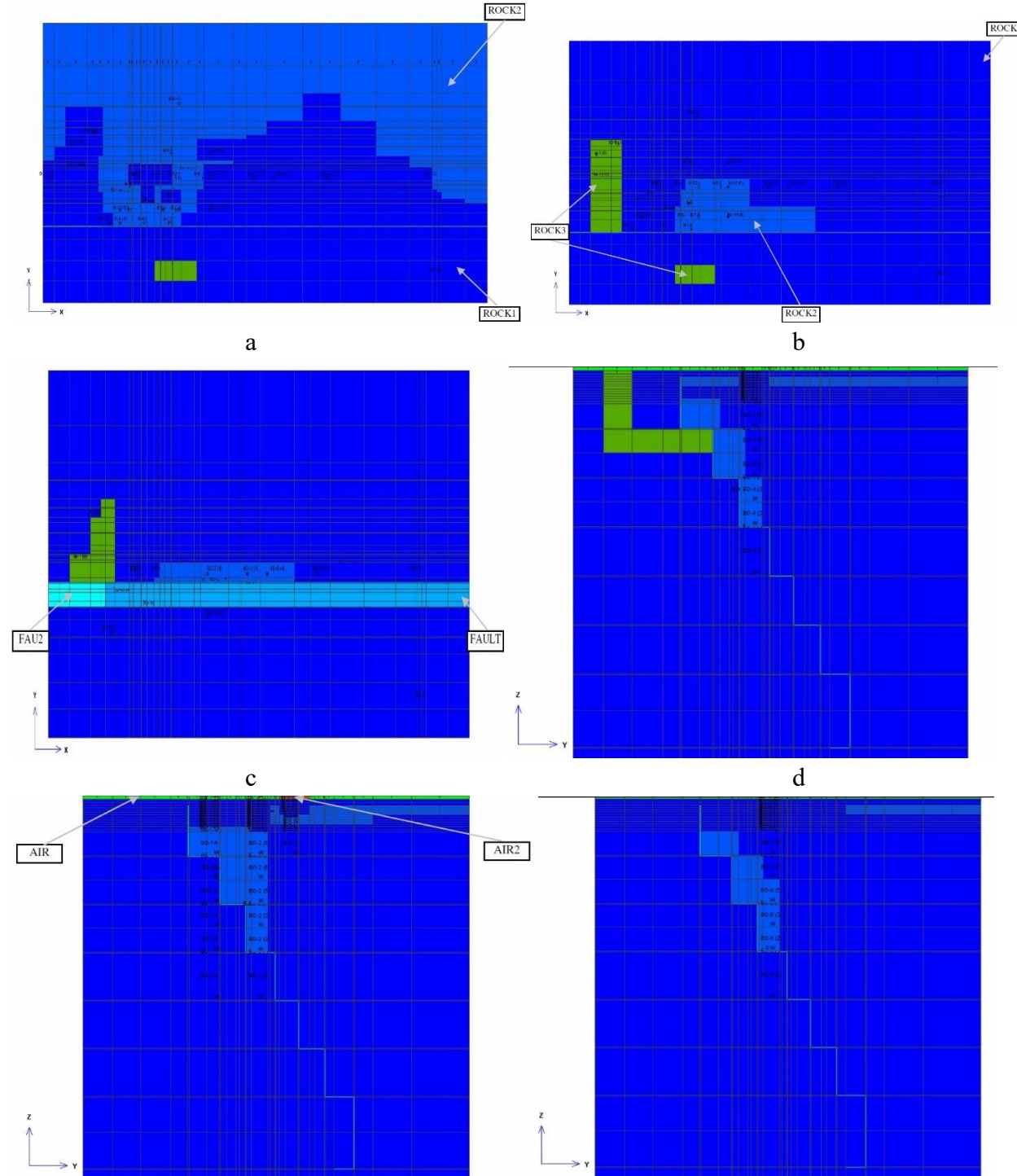


Figure 23. Production/injection well scheme for Scenario-III

CHAPTER 5: RESULTS AND DISCUSSION

5.1 Model construction

All the 2D generated grid models results at various cross sections are illustrated in the Figures below.



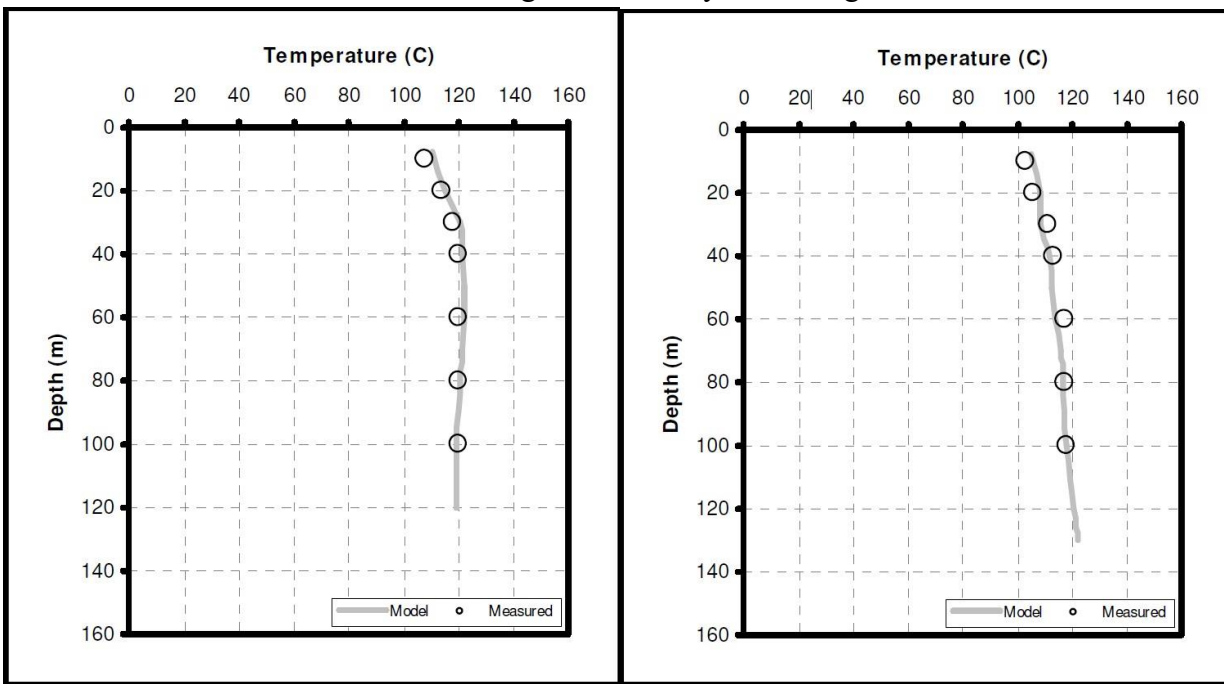
e

f

Figure 24. 2D grid model results displaying rock, fault and air distribution at various cross section (a indicates cross section $z=-15$, b indicates $z=-150$, c shows $z=-400$, d displays $x=3075$, e shows $x=3470$ and f indicates $x=3920$)

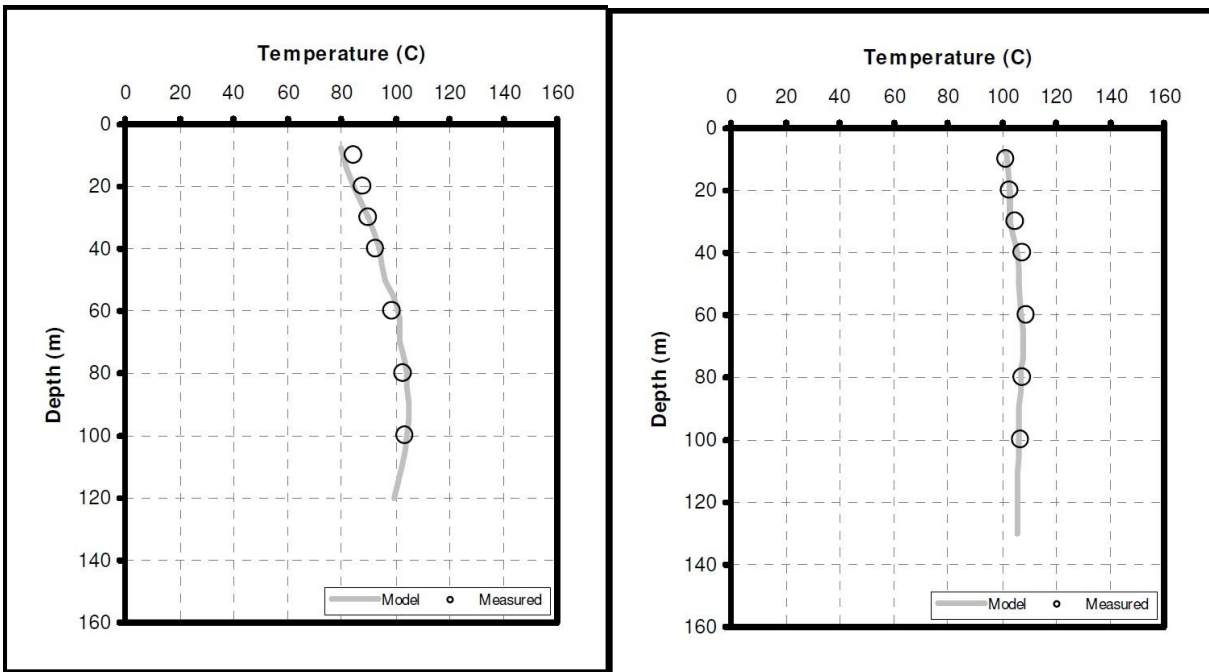
5.2 Natural state modelling

The temperature profiles of several wells derived from natural state modeling and actual temperature profiles are compared in (Figure 25). The bold steady line in these graphs displays model data, whereas the circles indicate measured or actual data. The outcomes of the model and the measured data are seen to correspond fairly well. Wells B-11 and BD-1 only have very slight variation in simulated and measured data beginning from depths 60m and 400m, respectively. However, these variations can still be neglected, as they are not significant.

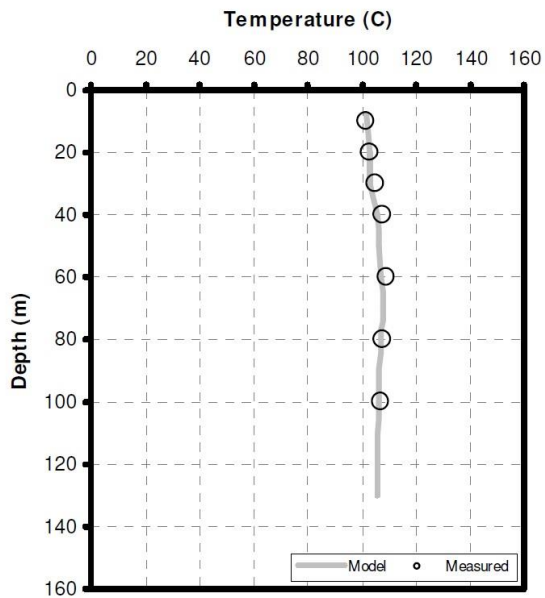


a) B-4

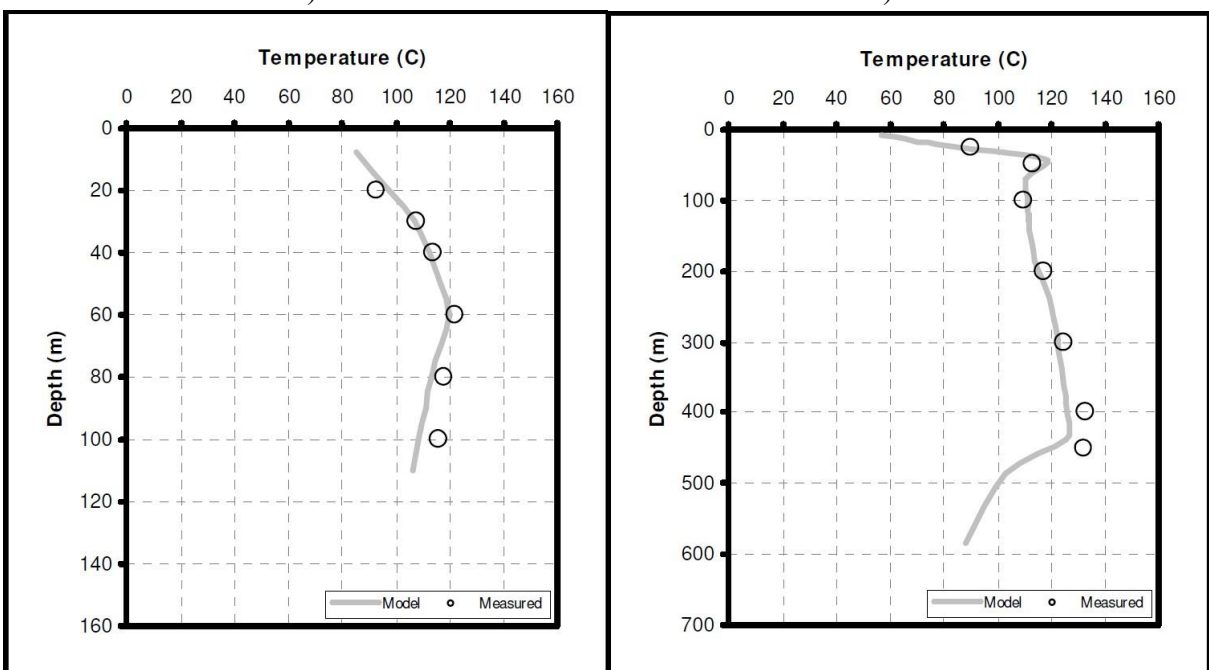
b) B-7



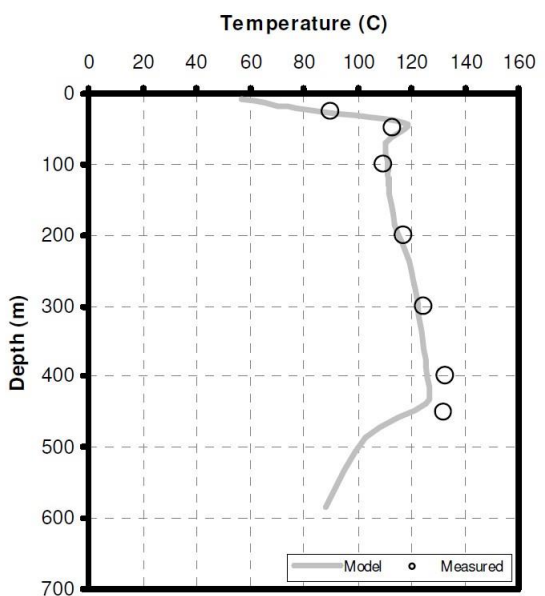
b) B-8



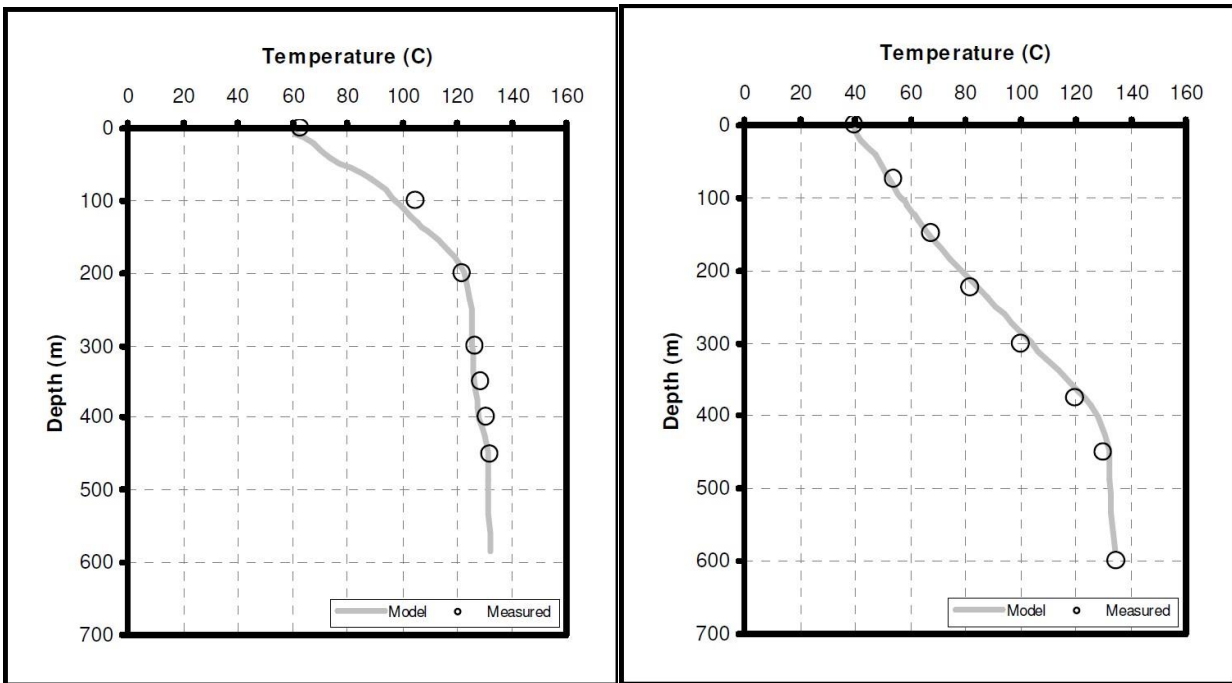
d) B-10A



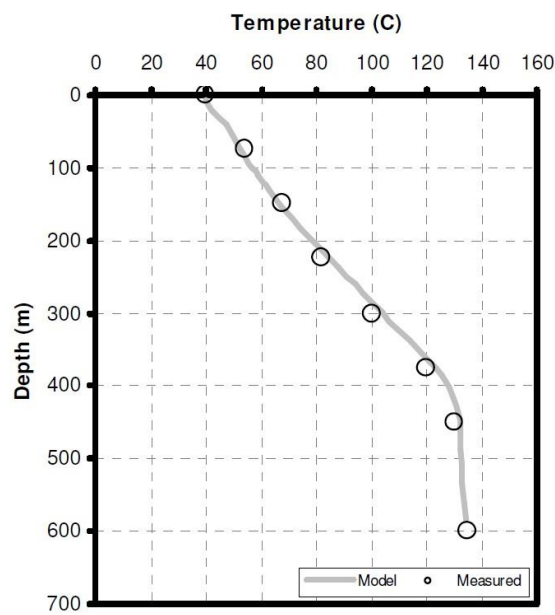
e) B-11



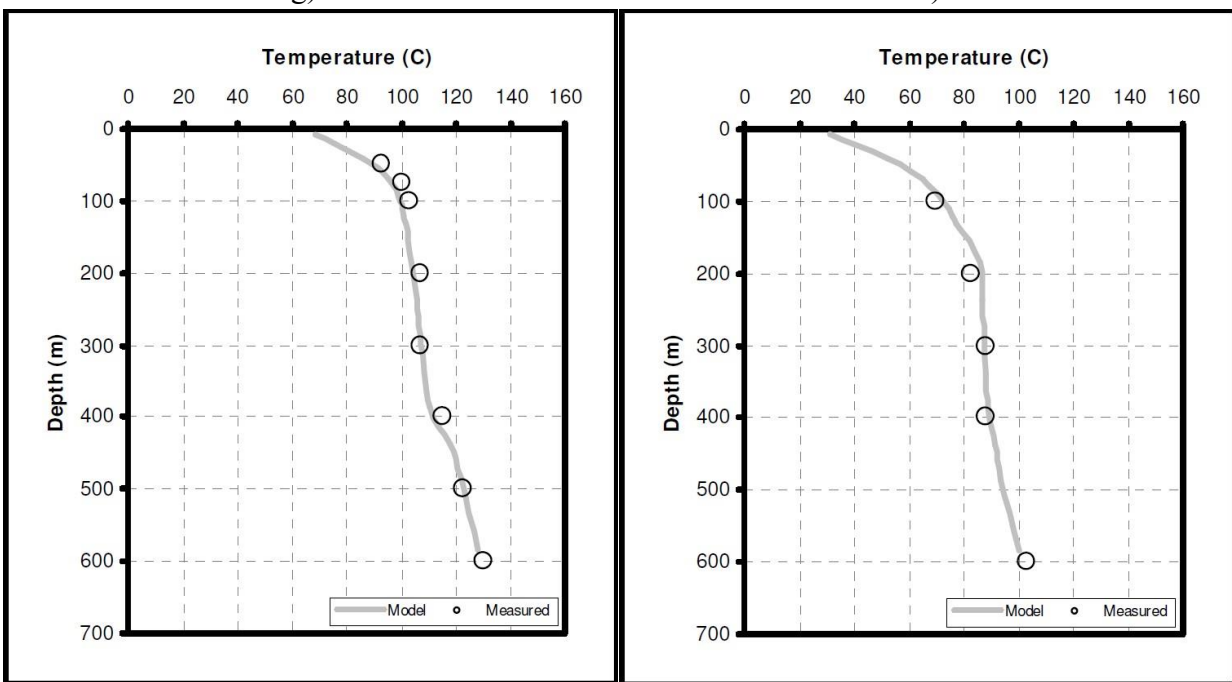
f) BD-1



g) BD-2

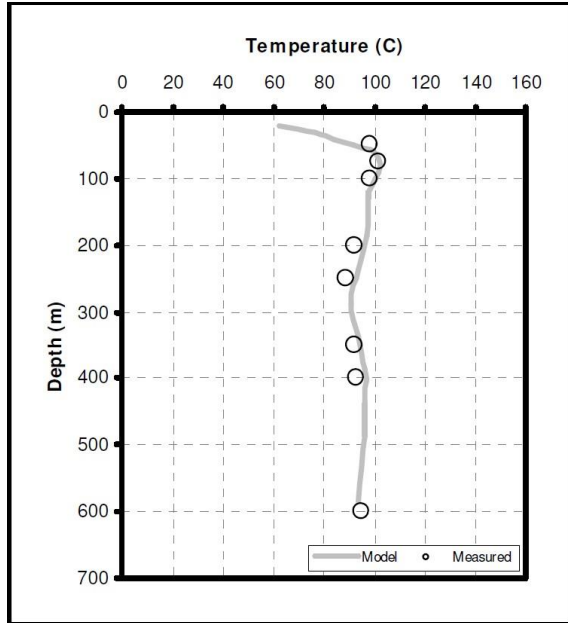


h) BD-3



i) BD-4A

j) BD-5



k) ND-1

Figure 25. Distribution of modelled and measured temperature values with depth for shallow and deep wells.

The quality of good match of modelled and actual temperature values at natural state can also be seen from Figure 26. Here it is obvious how they are scattered together along the line of 45°. As stated before, here there is negligibly slight inclination from actual data in well BD-1 only.

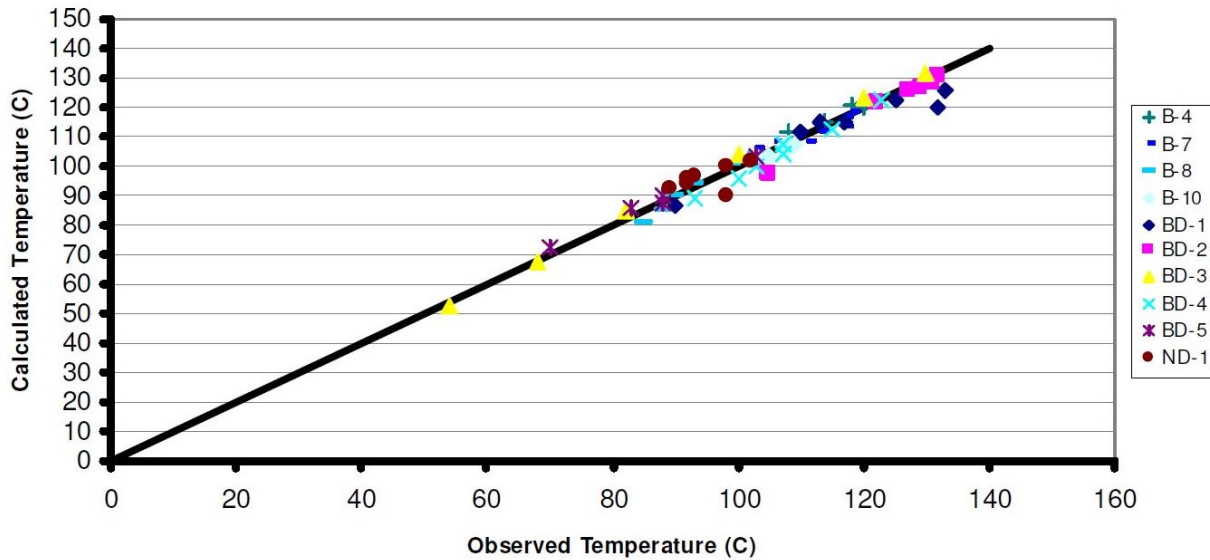
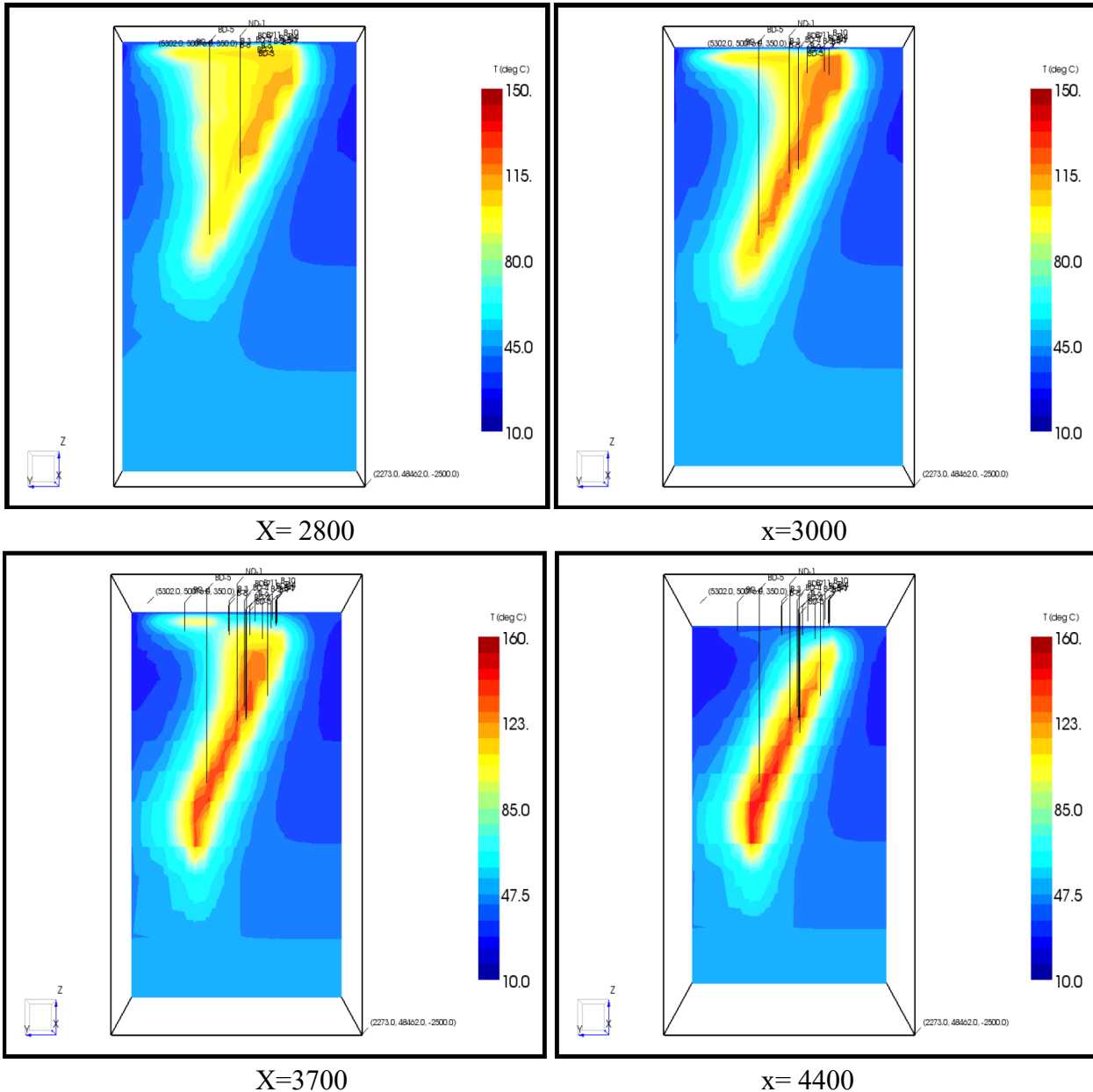


Figure 26. Comparison between modelled and measured temperature values at natural state.

The Figure 27 represents the captured images of initial temperature layout throughout the BNGF. Here, the temperature distribution is examined at certain cross sections (in X and Z directions

separately). According to the Figure below, the temperature of hot water is highest at cross sections $x=3700$ and $x=4400$, while the lowest temperature corresponds to cross section at $x=2800$. It implies that the temperature of hot water entering in the eastern part of the field decreases towards the western part of it. Moreover, it can be noticed from areal temperature layout (in Z direction) that the hot water loses a portion of its energy when it travels upwards (from $z=-550$ till $z=0$). The hottest part is observed in close to the layer of lower permeability in the center of the field.



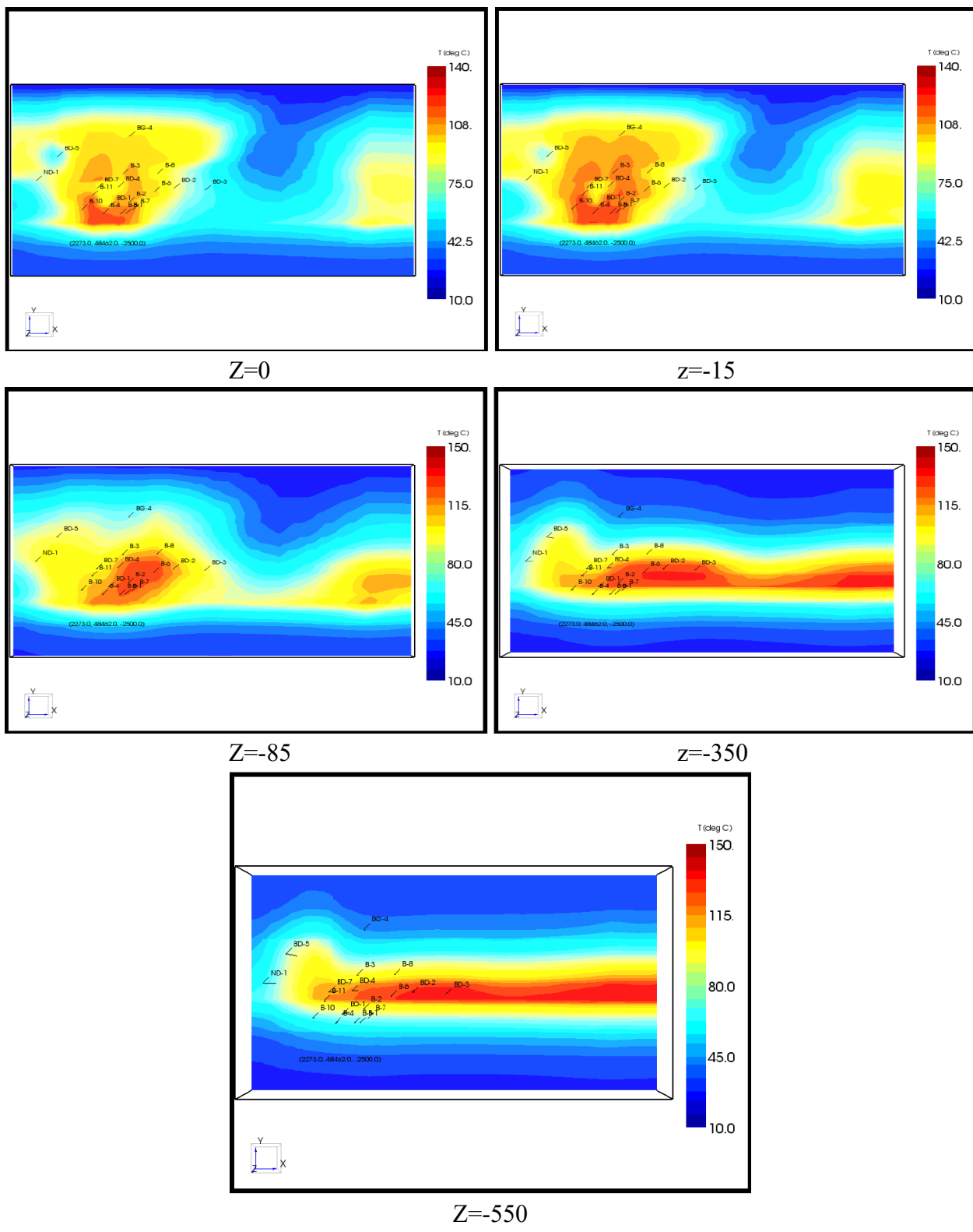
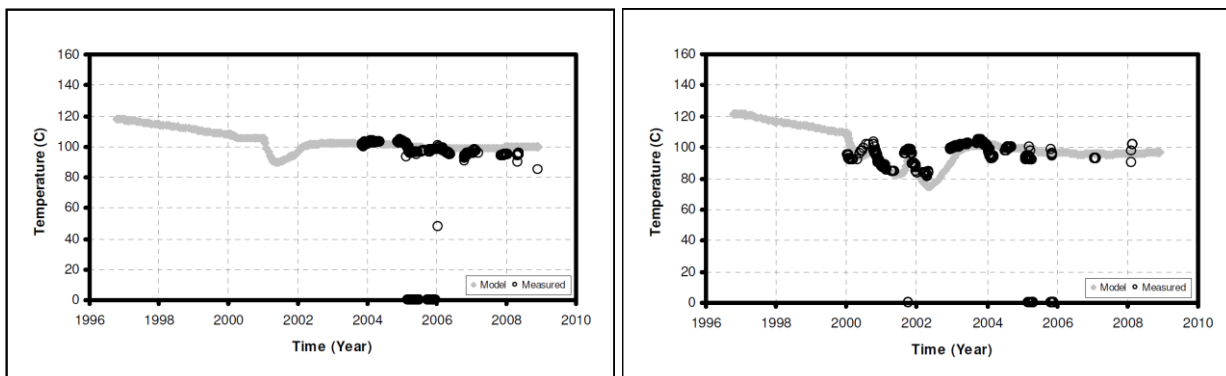


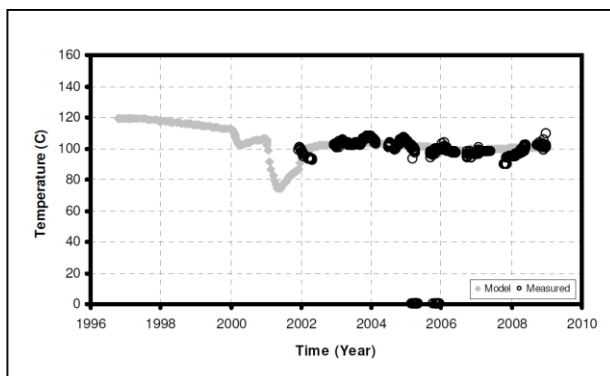
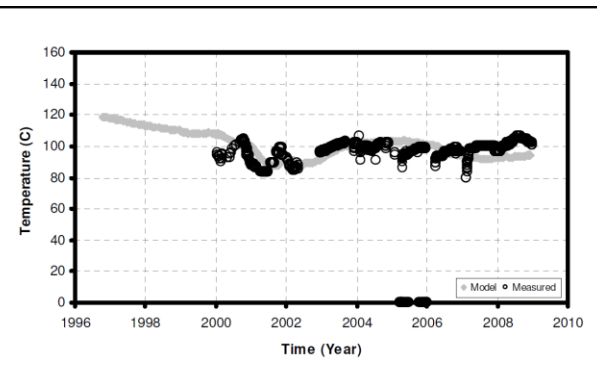
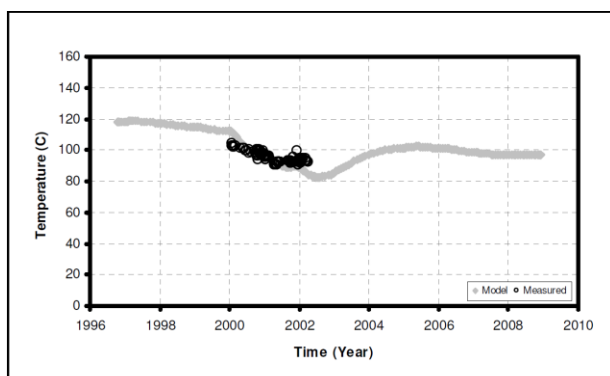
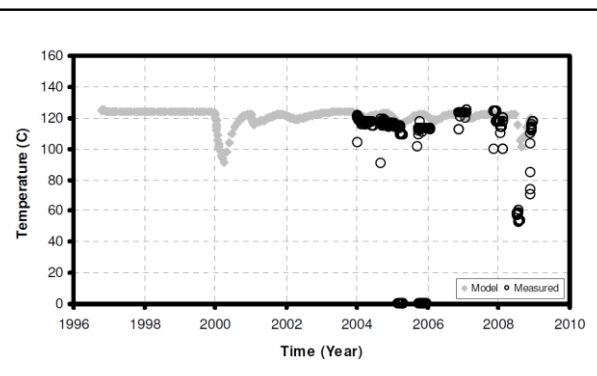
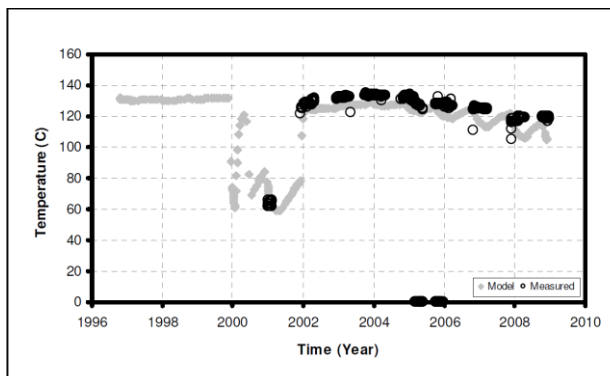
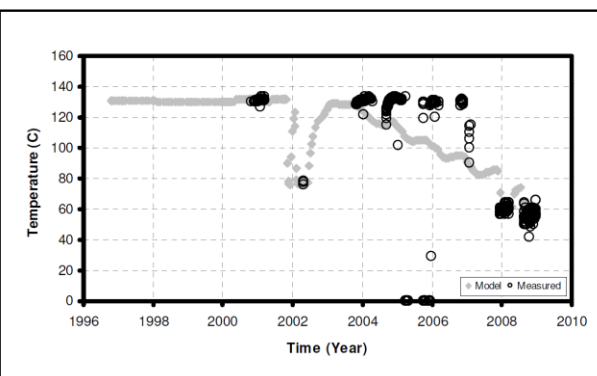
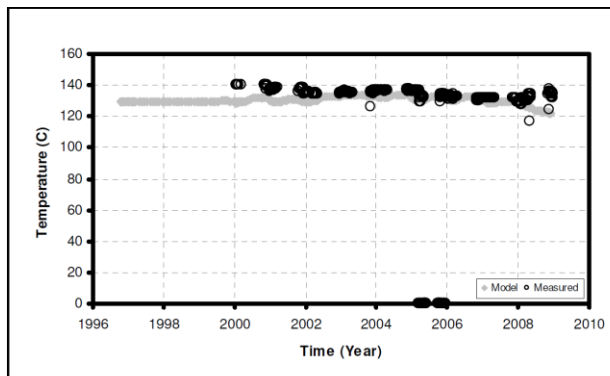
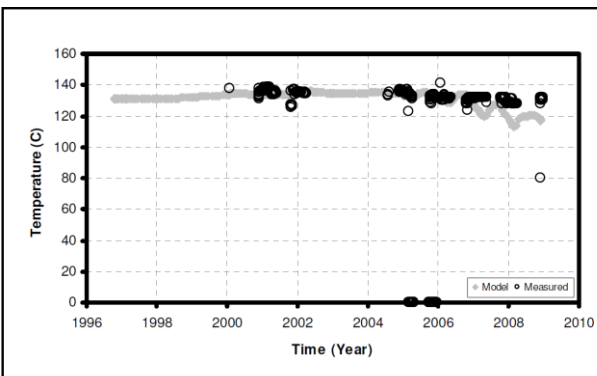
Figure 27. Temperature distribution at natural state in BNGF at various cross sections.

5.3 History matching

In this stage of geothermal reservoir simulation, several iterations and parameter calibrations have been performed until obtaining the match in production history data. The initial mass flow rate of hot water was assigned at 50kg/s and this was found to be insufficient to maintain the high rate of produced fluid. As a result, in natural state modeling, the boundary condition for the cells that received hot water injection was altered to a fixed state option. So, the rate of hot water that enters AG-I fault has been increased considering the pressure decrease due to production. In history matching investigations, cold water recharge to shallow depths was also used. The recharge cold water starts at the surface in the southern part of AG-I fault and exits the geothermal system at a shallow depth of 200m when it crosses the AG-I fault. Temperature drop in well B-10A has been observed as a result of early production along with the shallow injection through the well B-9. Moreover, temperature in wells B-1 and B-7 decreased too. Considering that these two wells have no association with the injection through well B-9, it has been deduced that there was an invasion of cold water caused by the pressure drop in the region because of heavy production. The formation Rock3 designates the area where cold water travels. For the cells that are near the surface, the fixed state option was used to control the entry of cold water. The pressure and temperature of the fixe state cell are 6.2×10^6 Pa and 10°C, respectively.

Bottomhole temperature results from the model study were compared to measurements made between 1996 and 2010 (Figure 28). The continuous bold line represents the model data while the points indicate measured values. It can be seen from plots that there is an adequate fit between actual and simulated data. Having noted that, there are just few deviations from the measured data in wells BD-3 and BD-1. The well BD-8 well was used for the majority of injections, after 2003. When examining the impact of the BD-8 well on the BD-2 well, it can be argued that the temperature reduction in the BD-3 well was inevitable given that it is situated closer to the BD-8 well. Moreover, sudden temperature drop has been observed in well BD-3 beginning from 2003. The reason for that is that the well BD-8 used for reinjection purposes is located close to well BD-3. The quality of good match of modelled and actual temperature values at natural state can also be seen from Figure 29. Here it is obvious how they are aligned together along the line of 45°. Few deviations can be seen in data of well BD-3.



B-1**B-4****B-5****B-10A****B-11****BD-1****BD-2****BD-3**

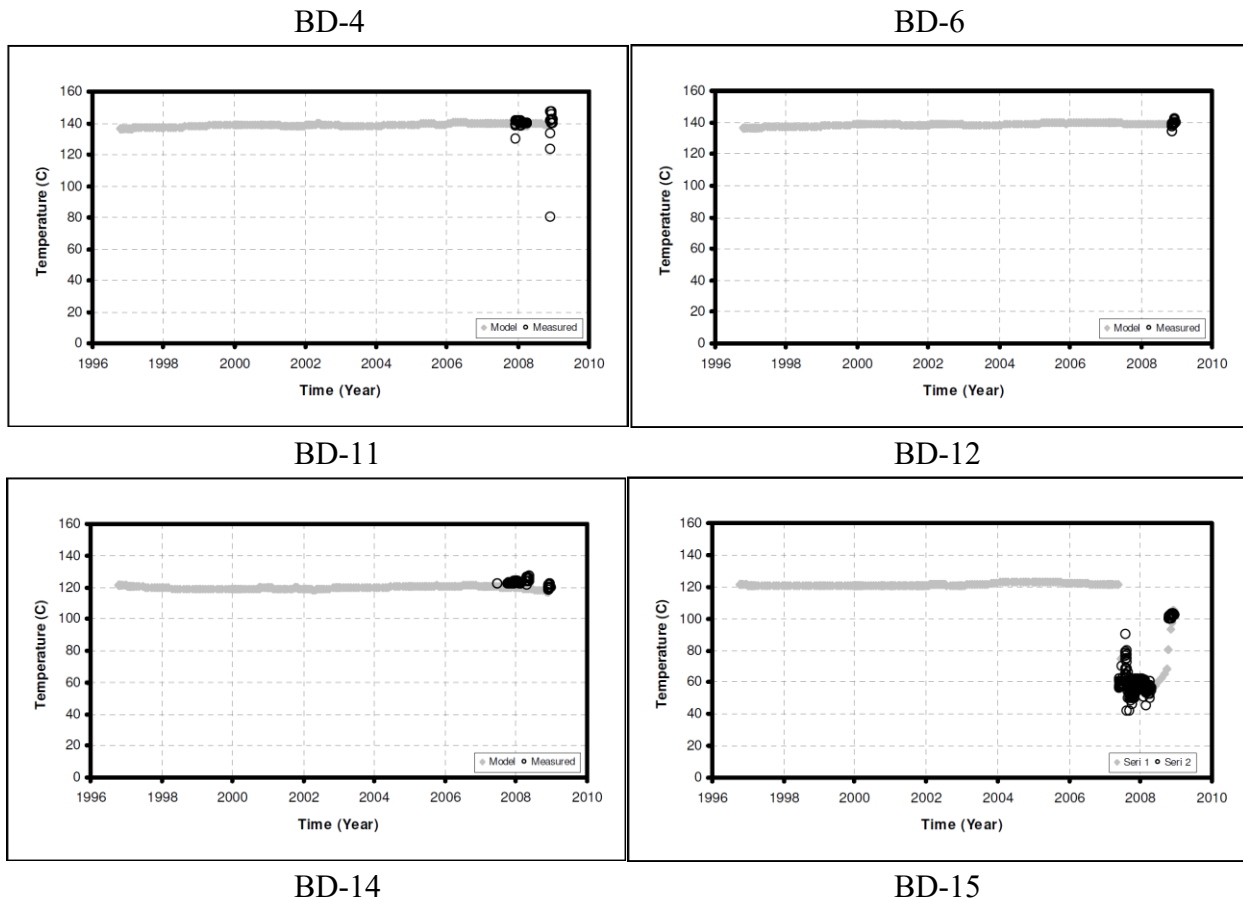


Figure 28. The Distribution of modelled and measured temperature values for shallow and deep wells for 13 years period.

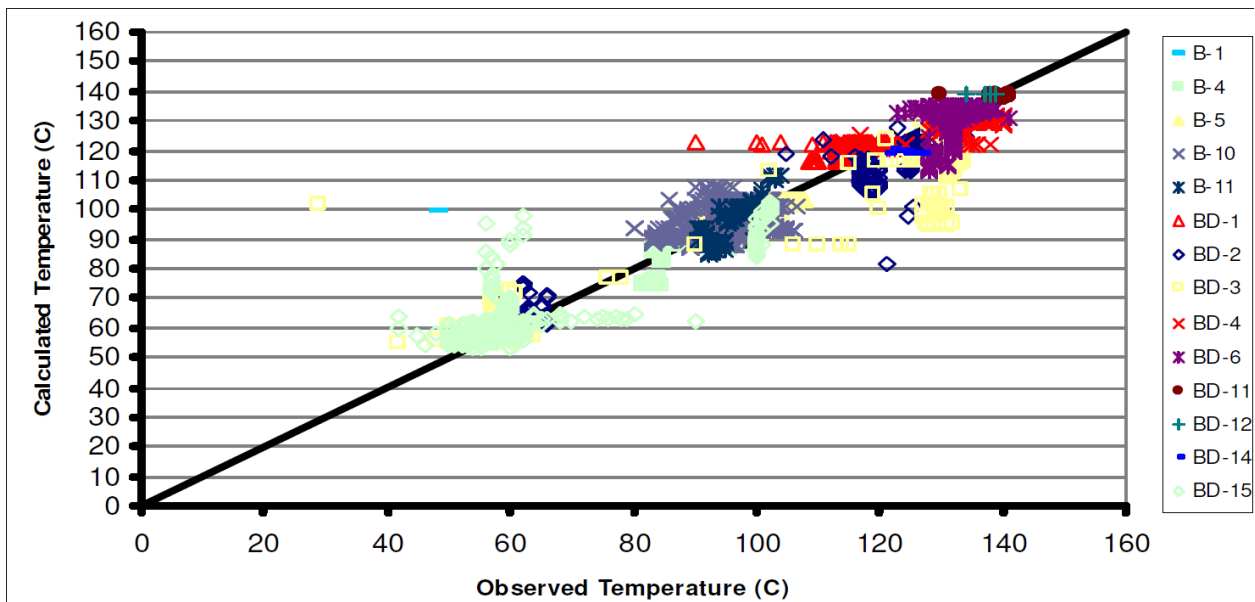


Figure 29. Comparison between modelled and measured temperature values during production-injection period.

5.4 Production and reinjection data history

The (Table 5) demonstrates annual outcomes of BNGF between years 2014-2021. It shows total electricity amount consumed in the Balçova-Narlıdere region including districts, buildings and energy needed for the field itself to operate. Throughout years the electricity has been consumed in almost the same amount of about 5000-6000Mwh, except in 2020. In 2020, electricity amount consumed was about 1500Mwh, as the worldwide pandemic affected workplaces and the field itself too. The total produced geothermal water volume is about $4.5 \times 10^6 \text{ m}^3$ in average from 2014 till 2021. Annual produced heat amount during these 8 years is approximately 300,000 Mwh/month. Volume of water reinjected into reservoir reaches in average about $4.2 \times 10^6 \text{ m}^3$ and constitutes nearly 93-95% of the total produced volume. Also, total freshwater consumption, Specific Energy, which is the electric energy consumed for the unit produced heat energy are indicated in the table below.

Table 5. Cumulative amount of water produced and reinjected in BNGF in years between 2014-2021.

Years	2014	2015	2016	2017
Total electricity consumption (Kwh)	3,635,945	5,689,614	5,796,387	5,875,420
Total freshwater consumption (m^3)	4,328	8,091	7,755	7,755
Total amount of produced water (m^3)	4,130,457	4,771,048	4,460,605	4,460,605
Total amount of heat produced (Mwh/month)	294,458	342,057	309,418	309,418
Total amount of reinjected water (m^3)	3,843,206	4,499,099	4,222,163	4,222,163
Reinjection percentage (%)	93.0	94.3%	94.7%	94.7%
Specific Energy (kWhe/mWht)	12.35	16.63	18.7	18.7
Average outside temperature ($^{\circ}\text{C}$)	17.2	17.0	17.4	17.4

Years	2018	2019	2020	2021
Total electricity consumption (Kwh)	4,031,353	5,196,523	1,479,822	5,273,283
Total freshwater consumption (m^3)	6,320	5,156	3,623	3,525
Total amount of produced water (m^3)	4,464,591	4,725,766	4,580,495	4,232,703

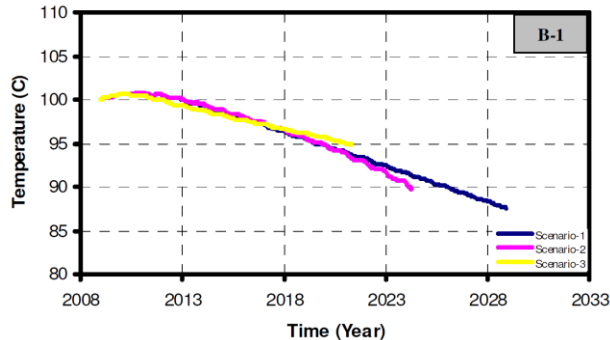
Total amount of heat produced (Mwh/month)	302,927	320,855	313,519	295,269
Total amount of reinjected water (m³)	4,288,500	4,505,600	4,211,332	4,041,092
Reinjection percentage (%)	96.1%	95.3%	91.94%	95.4%
Specific Energy (kWhe/mWht)	13,3	16.2	211.9	267
Average outside temperature (°C)	17.8	17.4	11.5	10.8

5.5 Forecasting

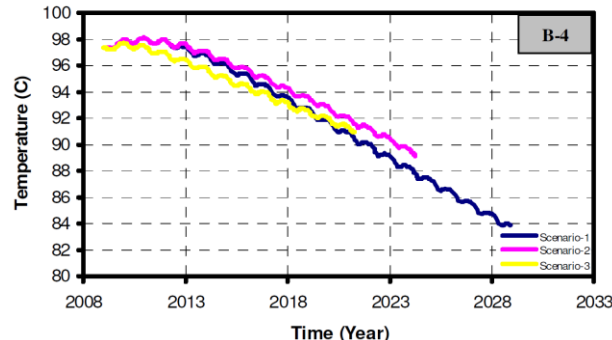
Results obtained at the end of simulation and the discussion of all three scenarios have been implemented in this part of research. From (Figure 30), it is obvious that there are no big changes between all three scenarios for wells B-1, B-5, BD-1 and B-4. Moreover, while discussing changes occurring between scenarios, Scenario-I can be chosen as a reference scenario in some manner. As the major injection well in each of scenarios are in the far distance from these wells the effect of injection wells is not significant on them. Looking at the plot of well BD-2, in Scenario-III, the temperature of the well increased due to effect of injector BT-1, which is located close to BD-2. Due to their alignment on the same E-W line, BD-8 and BD-2 must have been impacted by the AG-I fault. Compared to the outcomes of Scenario-I and Scenario-III, in Scenario-II, the temperature of wells BD-12, BD-9 and BD-11 dropped steadily, which shows that they are heavily influenced by the effect of continuous increase of production wells and injector BD-8. When it is switched from Scenario-I to Scenario-II, wells BD-4, BD-6 experienced cooling, while in the Scenario-III, it is vice versa for the well BD-6 as there is a temperature increment. However, injecting from BT-1, in Scenario-III, resulted in temperature drop in well BD-4.

(Figure 31) represents the bottomhole pressure lines of certain wells derived after simulation run for each of three scenarios. Looking carefully, it can be noticed that there is no significant change in all scenarios for wells BD-15, BD-5, BD-1 and BD-7. The reason for that is that they are not located close to major production and injection wells. However, in Scenario-II, the bottomhole pressures of wells BD-2, BD-6, BD-1, BD-11, BD-1, BD-14, and BD-14 have increased. As stated in Scenario-II, when the producer and injector locations are unchanged, the injection volume increase is always greater than the producer volume increase. Thus, as more water was injected over time, the pressure in the wells closest to the injection wells BD-3 and BD-8 increased. When Scenario-II was applied, the bottomhole pressure in wells B-5 and B-10A showed a reduction. Wells B-5 and B-10A are field's top shallow production wells. These two

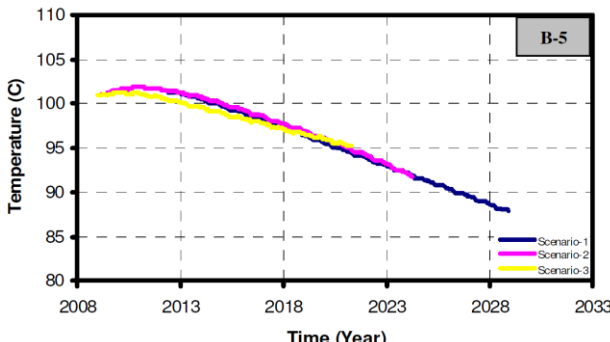
wells' pressure levels could not be maintained by longer higher-rate production or by using injection techniques from deeper reservoir portions.



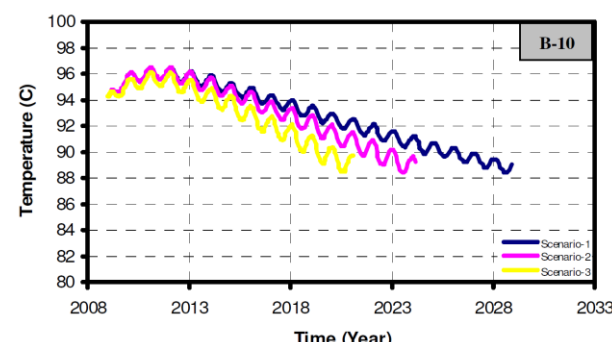
B-1



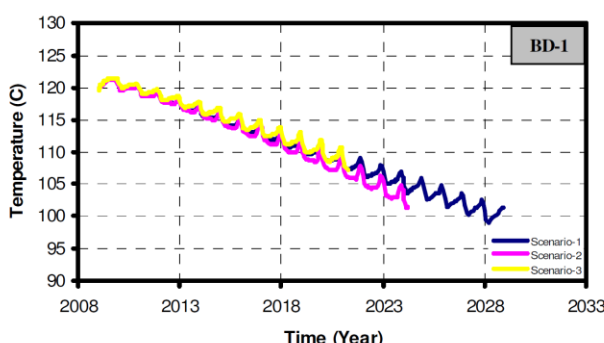
B-4



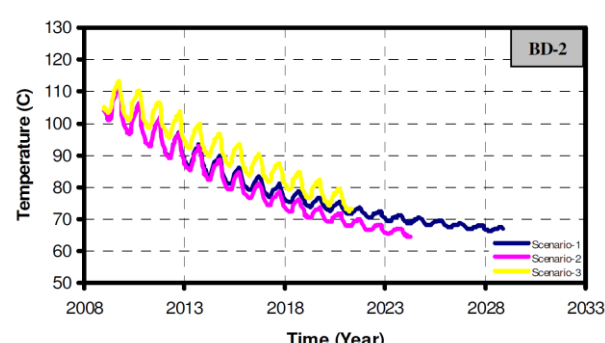
B-5



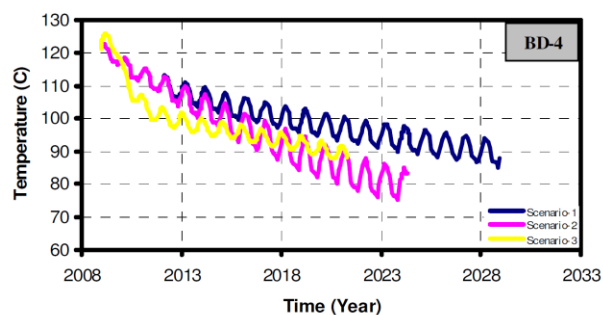
B-10A



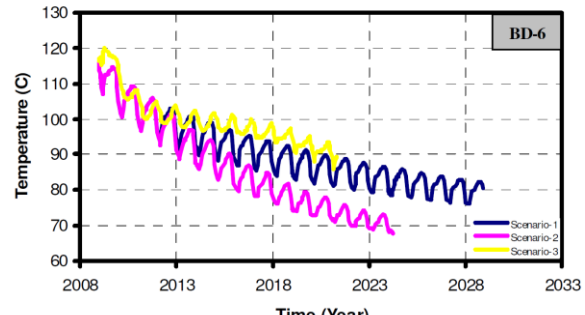
BD-1



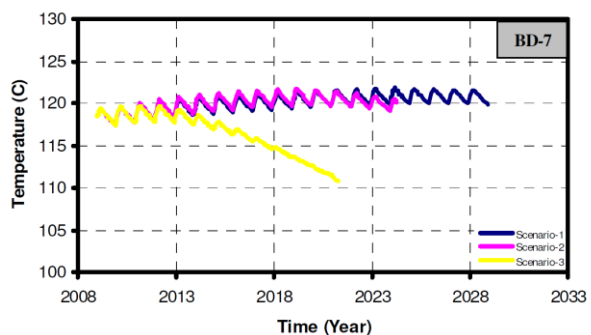
BD-2



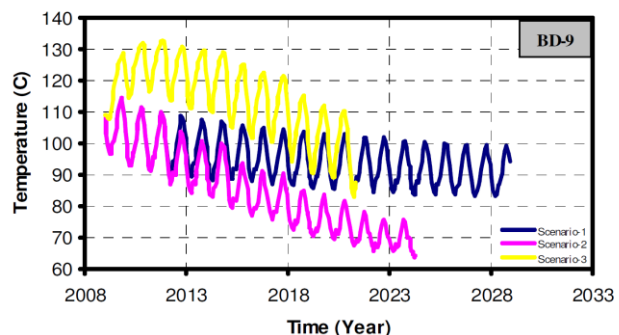
BD-4



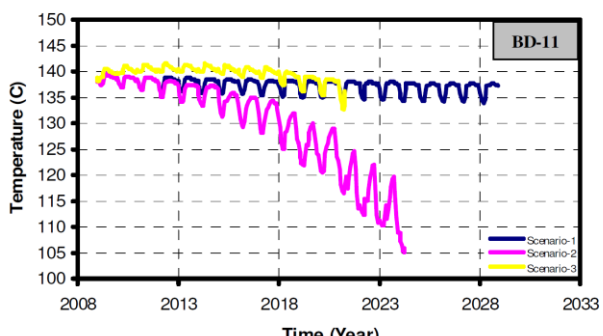
BD-6



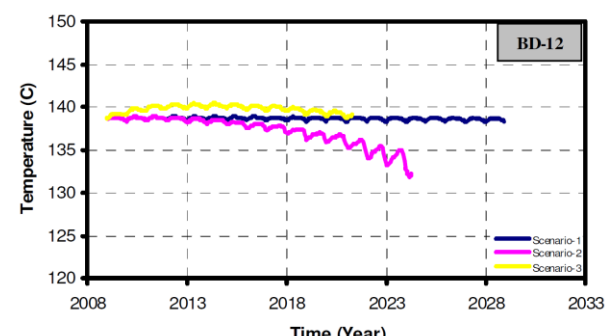
BD-7



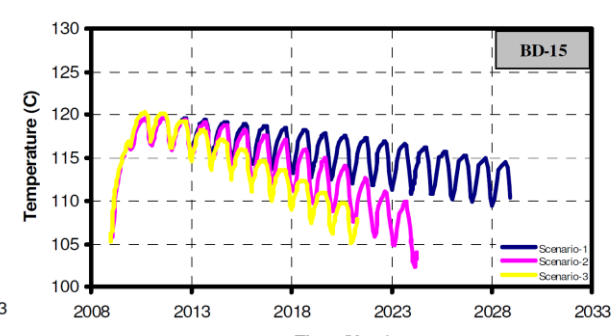
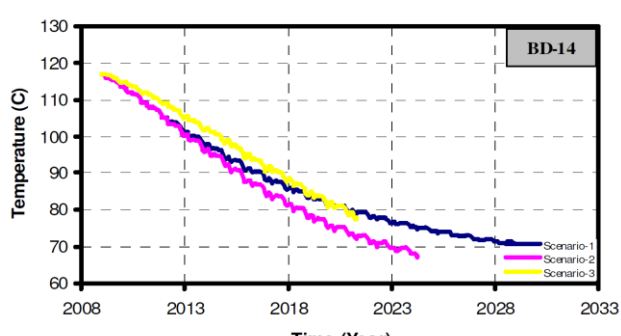
BD-9



BD-11



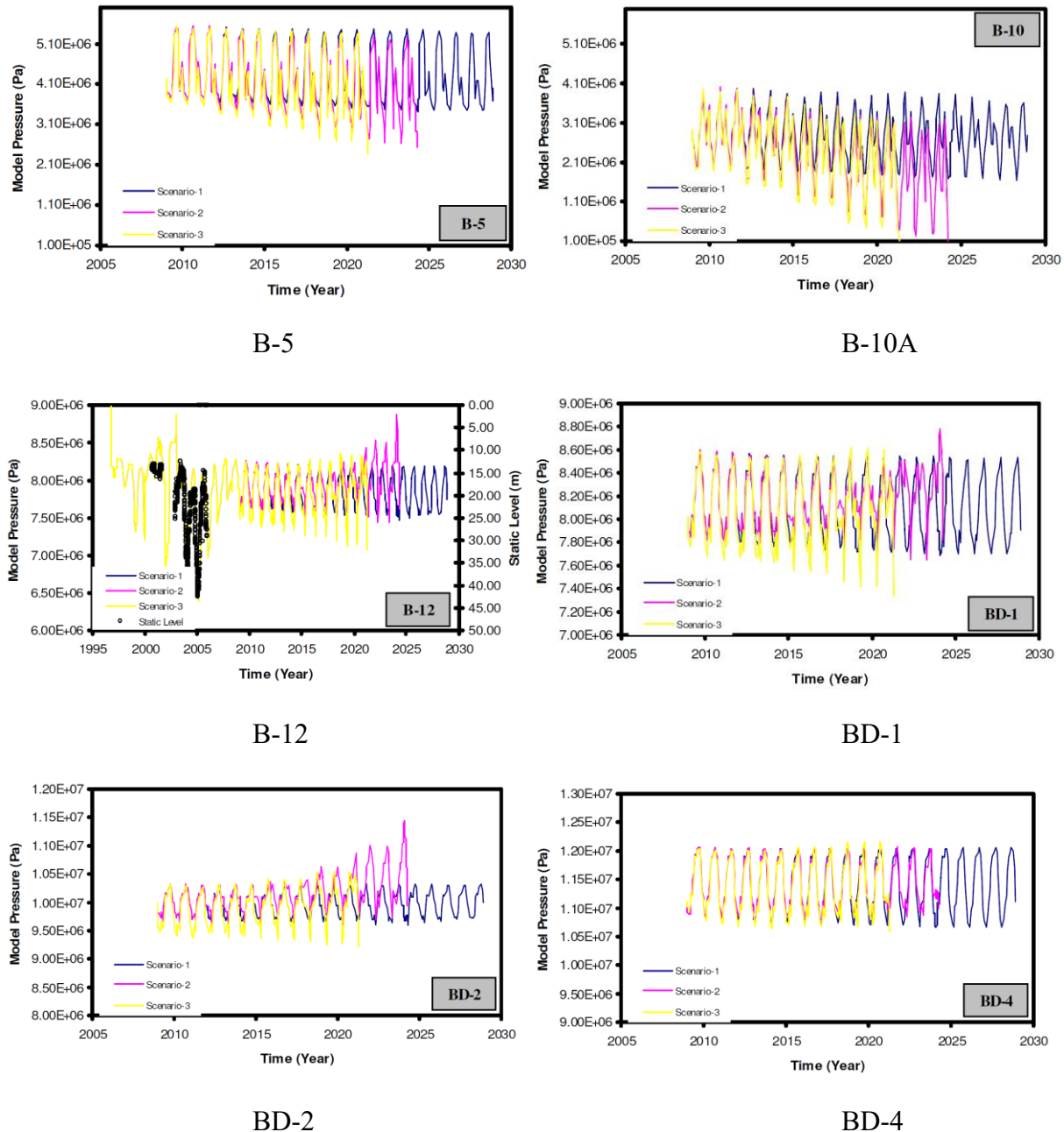
BD-12



BD-14

BD-15

Figure 30. Bottomhole temperature results derived from simulation run for all three scenarios.



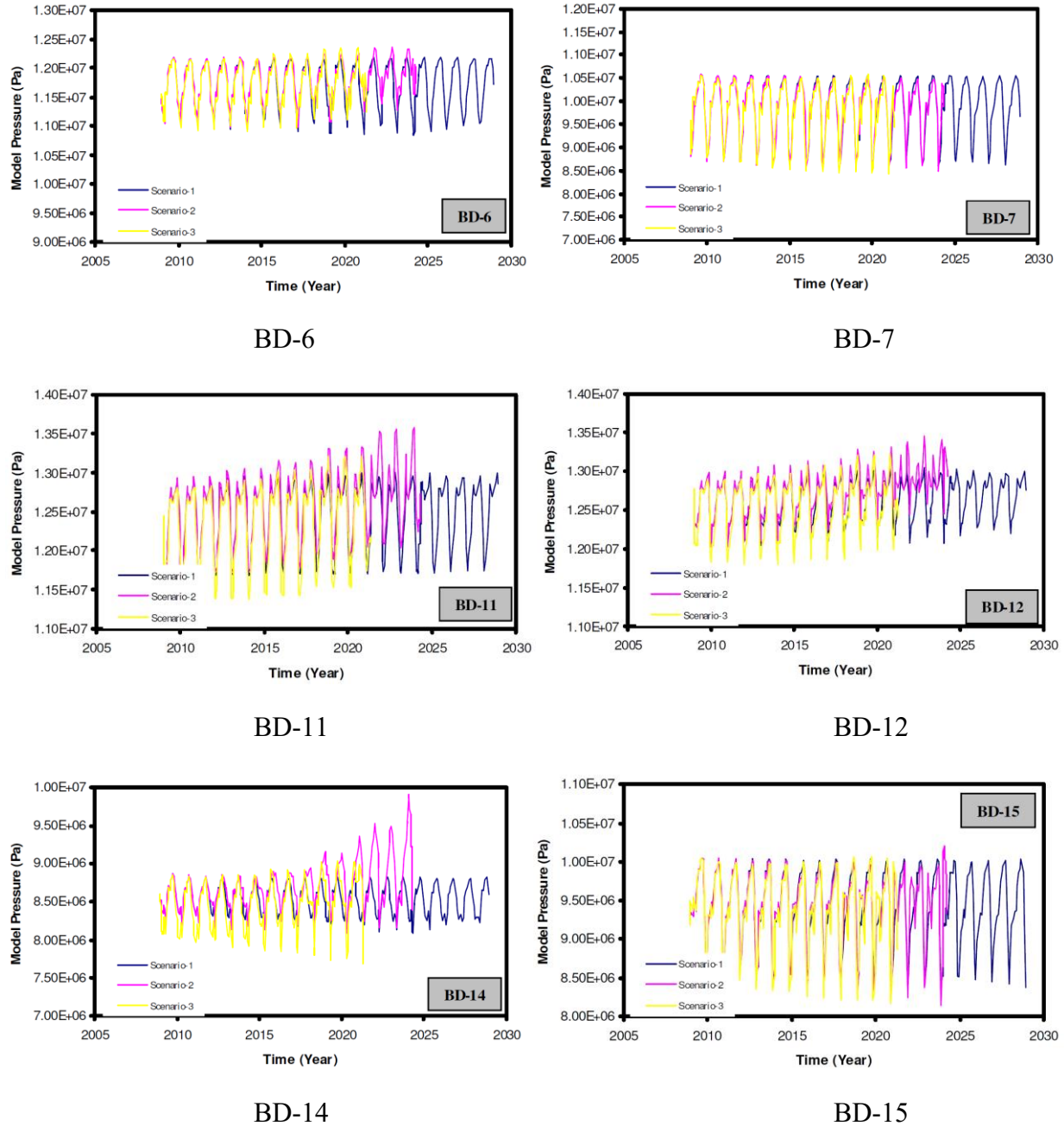


Figure 31. Bottomhole pressure results derived from simulation run for all three scenarios.

CHAPTER 6: CONCLUSION

The principal conclusions drawn from this research have been listed in the following way:

- The production and injection history match and natural state modelling have been accomplished successfully.
- According to the results of future performance prediction, the following conclusion have been made made:
 - ❖ In all three scenarios, all the production wells experienced temperature drop. In Scenario-II, bottomhole temperature values for deep wells BD-9, BD-2, BD-11, BD-6, BD-12 which are in the eastern part of BNGF and values of deep wells BD-5, BD-4, BD-7, BD-15 which are located in the western part of the BNGF diminished much lower than the temperature values of the same wells in the Scenario-I.
 - ❖ Compared to Scenario-I, in Scenario-III, temperature at western side wells decreased at high degree while the temperature of eastern side wells declined at lower degree.
 - ❖ Compared to Scenario-II, in Scenario-III, temperature at western side deep wells BD-7 and BD-15 dropped much.
 - ❖ Temperature variations between shallow wells have been observed to be insignificant in all the scenarios.
 - ❖ From results of all three scenarios, it can be deduced that there is no important change in bottomhole pressure in deep wells.
 - ❖ Compared to Scenario-I, in other two scenarios, the bottomhole pressure decreased in shallow wells B-10A and B-5. The reason is that the flow rate in these wells increase continuously while there is small effect of injection wells because of their deeper locations. The pressure decrease occurred more in Scenario-III than Scenario-II.
 - ❖ In the first two scenarios, water injected primarily through wells BD-3 and BD-8 prevented hot water flowing from deep areas and forced it to flow to the western side, where it heated that area. Nevertheless, it was found that in the Scenario-III, the water utilized for injection through the well BT-1 cooled the west and the deep regions where it was injected. The hot water travelled more eastward as the amount of water flowing in eastern direction reduced and the water amount moving in western direction increased.
 - ❖ When comparing the temperature quantities of the producers and the amounts of production from those wells in all three scenarios, it can be concluded that if the same production scenario as in 2008 is repeated, the reinjection procedure, which includes the well BT-1 drilled to the depth of 765 m, will likely result in

less cooling in the production zone. This implies that by using that new injector, additional energy will be collected from the field.

REFERENCES

- Baba, A., Sözbilir, H., Sayık, T., Arslan, S., Uzelli, T., Tonkul, S., & Demir, M. M. (2022). Hydrogeology and hydrogeochemistry of the geothermal systems and its direct use application: Balçova-Narlıdere geothermal system, İzmir, Turkey. *Geothermics*, 104. <https://doi.org/10.1016/j.geothermics.2022.102461>
- Başarır, & Konuk. (1981). Gümüldür yöresinin kristalin temeli ve allokton birimleri Crystalline basement and allochthonunits of Gümüldür region. In *Türkiye Jeoloji Kurumu Bülteni*, C (Vol. 24).
- Burhan Erdogan. (1990). İzmir-Ankara Zonu'nun, İzmir ile Seferihisar Arasındaki Bölgede Stratigrafik Özellikleri ve Tektonik Evrimi. TPJD Bülteni, 2/1. *Turkish Association of Petroleum Geologists*, 2(1), 1–21.
- Emre, Ö., Özalp, S., Doğan, A., Özaksoy, V., Yıldırım, C., & Göktaş, F. (2005). *İZMİR YAKIN ÇEVRESİNİN DİRİ FAYLARI VE DEPREM POTANSİYELLERİ MADEN TETKİK VE ARAMA GENEL MÜDÜRLÜĞÜ*.
- Gessner, K., Gallardo, L. A., Markwitz, V., Ring, U., & Thomson, S. N. (2013). What caused the denudation of the Menderes Massif: Review of crustal evolution, lithosphere structure, and dynamic topography in southwest Turkey. *Gondwana Research*, 24(1), 243–274. <https://doi.org/10.1016/J.GR.2013.01.005>
- Hasan SÖZBİLİR, & Prof. Dr. BABA, A. (2016). *Balçova (İzmir) 2064, 2065, 2081, 2087, 2094, 2161 ve 2141 Numaralı İşletme Ruhsatlarına İlişkin Kaynak Koruma Alanı Etüt Raporu*.
- Kömürçü, M. I., & Akpinar, A. (2009). Importance of geothermal energy and its environmental effects in Turkey. *Renewable Energy*, 34(6), 1611–1615. <https://doi.org/10.1016/j.renene.2008.11.012>
- MTA Genel Müdürlüğü. (2022). <https://www.mta.gov.tr/v3.0/arastirmalar/jeotermal-enerji-arastirmaları>
- PetraSim - RockWare. (2022). <https://www.rockware.com/product/petasim/>
- PRUESS, K., SIMMONS, A., Y.S. Wu, & MORIOIS, G. (1996). *TOUGH2 Software Qualification*.
- Sari, B. (2013). Late Maastrichtian-Late Palaeocene planktic foraminiferal biostratigraphy of the matrix of the Bornova Flysch Zone around Bornova (İzmir, Western Anatolia, Turkey). *Turkish Journal of Earth Sciences*, 22(1), 143–171. <https://doi.org/10.3906/YER-1107-2>
- Sözbilir, H., Sari, B., Uzel, B., Sümer, Ö., & Akkiraz, S. (2011). Tectonic implications of transtensional supradetachment basin development in an extension-parallel transfer zone: the Kocacay Basin, western Anatolia, Turkey. *Basin Research*, 23(4), 423–448. <https://doi.org/10.1111/J.1365-2117.2010.00496.X>
- Sözbilir, H., Uzel, B., Sümer, Ö., Ersoy, E. Y., Koçer, T., Demirtaş, R., Özkaraymak, Ç., Eylül Üniversitesi, D., Mühendisli, J., Yerleükesi, K., & -ØZMØR, B. (2008). D-B Uzanmlı İzmir Fay İle KD-Uzanaklı Seferihisar Fayının Birlikte Çalışlığına Dair Veriler: İzmir Körfezi'ni Oluşturan Aktif Faylarda Kinematik Ve Paleosismolojik Çalışmalar, Batı Anadolu. *Türkiye Jeoloji Bülteni*, 51(2), 91–114. <https://dergipark.org.tr/tr/pub/tjb/issue/28370/301652>

Tepe, Ç., Sözbilir, H., Eski, S., Sümer, Ö., & Özkaymak, Ç. (2021). Updated historical earthquake catalog of İzmir region (western Anatolia) and its importance for the determination of seismogenic source. *Turkish Journal of Earth Sciences*, 30(8), 779–805. <https://doi.org/10.3906/yer-2101-14>

TOUGH2 / PetroMehras Directory. (n.d.). Retrieved October 22, 2022, from <https://www.petromehras.com/petroleum-software-directory/reservoir-simulation-software/dynamic-simulation-software/tough2>

Uzel, B., Sözbilir, H., & Özkaymak, Ç. (2012). *Neotectonic Evolution of an Actively Growing Superimposed Basin in Western Anatolia: The Inner Bay of İzmir, Turkey*. <https://doi.org/10.3906/yer-0910-11>